Census of High- and Medium-mass Protostars. V. CO Abundance and the Galactic X_{CO} Factor

Rebecca L. Pitts[1,2] and Peter J. Barnes[2,3,4]

[1] Niels Bohr Institute, Centre for Star & Planet Formation, University of Copenhagen, Øster Voldgade 5–7, DK-1350 Copenhagen K, Denmark
rebecca.pitts@nbi.ku.dk
[2] Department of Astronomy, University of Florida, 211 Bryant Space Science Center, Gainesville, FL 32611, USA
[3] Space Science Institute, 4765 Walnut St., Suite B, Boulder, CO 80301, USA
[4] School of Science and Technology, University of New England, Armidale, NSW 2351, Australia

Abstract

We present the second dust continuum data release in the Census of High- and Medium-mass Protostars (CHaMP), expanding the methodology trialed in Pitts et al. to the entire CHaMP survey area ($280° < \ell < 300°$, $-4° < b < +2°$). This release includes maps of dust temperature (T_d), H_2 column density (N_{H_2}), gas-phase CO abundance, and temperature–density plots for every prestellar clump with Herschel coverage, showing no evidence of internal heating for most clumps in our sample. We show that CO abundance is a strong function of T_d and can be fit with a second-order polynomial in log-space, with a typical dispersion of a factor of 2–3. The CO abundance peaks at $20.0^{+0.4}_{-1.0}$ K with a value of $7.4^{+0.2}_{-0.3} \times 10^{-5}$ per H_2; the low T_d at which this maximal abundance occurs relative to laboratory results is likely due to interstellar UV bombardment in the largest survey fields. Finally, we show that, as predicted by theoretical literature and hinted at in previous studies of individual clouds, the conversion factor from integrated ^{12}CO line intensity ($I_{^{12}CO}$) to N_{H_2}, the X_{CO} factor, varies as a broken power law in $I_{^{12}CO}$ with a transition zone between 70 and 90 K km s^{-1}. The X_{CO} function we propose has $N_{H_2} \propto I_{^{12}CO}^{0.51}$ for $I_{^{12}CO} \lesssim 70$ K km s^{-1} and $N_{H_2} \propto I_{^{12}CO}^{2.3}$ for $I_{^{12}CO} \gtrsim 90$ K km s^{-1}. The high-$I_{^{12}CO}$ side should be generalizable with known adjustments for metallicity, but the influence of interstellar UV fields on the low-$I_{^{12}CO}$ side may be sample specific. We discuss how these results expand on previous works in the CHaMP series and help tie together observational, theoretical, and laboratory studies on CO over the past decade.

1. Introduction

The single greatest impediment to the study of star formation is the H_2 molecule's lack of a dipole moment. Stars form in dense clouds where most of the hydrogen is in the form of H_2 (Lada & Lada 2003), and H_2 lacks molecular transitions that can be excited at temperatures (1 to a few $\times 10$ K) typical of molecular gas in the prestellar and early protostellar phases of evolution. Astronomers must rely on alternative tracers to probe the physical, chemical, and kinematic conditions of the gas, assuming that these tracers are well coupled to the H_2. Without a direct way to test that assumption, a variety of physical and chemical conditions must be surveyed with as many relevant tracers as possible to find the limits of each tracer's utility.

The Census of High- and Medium-mass Protostars (CHaMP, Barnes et al. 2011, 2013; Ma et al. 2013; Barnes et al. 2016; Schap et al. 2017; Barnes et al. 2018, hereafter Papers I, I-B, II, III, III-B, and IV, respectively) is one such survey focused on the upper end of the protostellar mass spectrum, where observations are further complicated by short formation timescales ($t \lesssim 10^6$ yr; e.g., Kahn 1974; Schaller et al. 1992; Kuiper et al. 2011; Yusof et al. 2013), large distances (>400 pc) to the nearest objects (see, e.g., Reid et al. 2009), and the crowded fields of the Galactic plane (see, e.g., review by Zinnecker & Yorke 2007). The CHaMP survey sample consists of about 300 clump- to core-scale (~ 1 to ~ 0.1 pc) condensations in the Carina −Sagittarius Arm within the $280° < \ell < 300°$, $-4° < b < +2°$

area, mapped with the Mopra[5] 22 m telescope in over 30 molecular species. Aside from questions more specific to massive star formation, like the duration of the prestellar phase, the CHaMP project's goals have expanded to include addressing more fundamental concerns about how common H_2 tracers, like CO($J = 1 - 0$) emission, change in their tracing efficacy with the physical conditions. Combining the multi-isotopologue CO data released in Paper III and Paper IV with archival dust continuum data from Herschel and other infrared observatories gave us the chance to begin exploring the detailed, temperature-dependent behavior of CO emission in Pitts et al. (2019, hereafter PBV19). In this study, we expand that work to the rest of the CHaMP sample.

Our previous and current works began, as many continuum surveys do, with fitting modified Planck spectral energy distributions (SEDs) in the manner of Hildebrand (1983), followed by detailed examination of the resulting maps of dust temperature (T_d) and H_2 column density (N_{H_2}). Similar work has been done as part of surveys like HiGAL (Peretto et al. 2010; Molinari et al. 2010a, 2010b, etc.) and MALT90 (Guzmán et al. 2015), and our work advances these studies

---

[5] The Mopra telescope is part of the Australia Telescope, funded by the Commonwealth of Australia for operation as a National Facility managed by CSIRO. The University of New South Wales Digital Filter Bank used for observations with the Mopra telescope was provided with support from the Australian Research Council.

with additional insights. T_d trends with N_{H_2} or with radial distance from the center of a condensation can indicate whether a clump is actively star-forming, and the proportion of clumps with cold versus warm centers is a proxy for the relative amounts of time spent in the prestellar and protostellar phases. Just within our survey, kinematic evidence from Paper III and Paper IV in the form of radial velocity shifts of ^{12}CO relative to ^{13}CO and C^{18}O suggested long infall timescales for prestellar clumps. This is further supported by the tendency of local N_{H_2} maxima to more often than not coincide with T_d minima found in PBV19. Most importantly, we used T_d and N_{H_2} from dust continuum emission, in conjunction with CO column densities derived using the three most abundant CO isotopologues (see Paper III for details), to derive gas-phase CO abundance (hereafter simply CO abundance) maps to relate to T_d and the integrated ^{12}CO line intensity ($I_{^{12}CO}$).

For most studies that do not focus on the behavior of CO as a function of local conditions, the usual method is to assume that the velocity-integrated intensity of the CO($J = 1 - 0$) line is proportional to the H_2 column density by some factor X_{CO} (Dame et al. 2001). Unlike H_2, the CO molecule's 3 mm $J = 1 - 0$ rotational transition is easily detectable with ground-based radio telescopes, and CO is the most abundant molecule in the universe after H_2. However, with full radiative transfer on multiple CO isotopologues (see Paper IV for details), the ^{12}CO($J = 1 - 0$) line is seen to be optically thick almost everywhere in the Galactic plane. Moreover, whenever X_{CO} is treated as a constant, typically averaging 2×10^{24} m^{-2} (K km s^{-1})$^{-1}$ to within a factor of 2 (Bolatto et al. 2013; Okamoto et al. 2017; Gong et al. 2018; Hayashi et al. 2019), it encodes a constant CO abundance of 10^{-4} per H_2. The inherent uncertainty in N_{H_2} derived from dust, by a factor of two to three owing to the uncertain gas-to-dust ratio (see, e.g., Beckwith et al. 1990; Zubko et al. 2004; Reach et al. 2015), is not nearly enough to explain the >2 order of magnitude variation seen in just the subset of CO abundance maps published in PBV19. A wide variety of both observational (Caselli et al. 1999; Bacmann et al. 2002; Hernandez et al. 2011; Fontani et al. 2012; Ripple et al. 2013; Kong et al. 2015) and laboratory (Öberg et al. 2009; Muñoz Caro et al. 2010, 2016; Noble et al. 2012; Cazaux et al. 2017) studies find that the CO abundance must vary with temperature and ambient radiation exposure. In this study we finally have the statistics to quantify the correlation of CO abundance with T_d in the Galactic plane. If CO abundance varies systematically with local physical conditions, there is no reason to believe that X_{CO} is constant, or that the argument from virialization is applicable.

Besides the obvious dependency of X_{CO} on metallicity, studies by Narayanan et al. (2011), Narayanan & Krumholz (2014), Barnes et al. (2015), Wada et al. (2018), Paper IV, and Sofue & Kohno (2020) found additional dependencies of X_{CO} on CO optical depth. The latter four papers, especially Barnes et al. (2015) and Paper IV, find that ^{13}CO and C^{18}O observations indicate that N_{CO} is higher than expected given I_{CO} in both the highest and lowest column density areas, such that the standard X_{CO} factor relationship can underpredict N_{H_2} by up to a factor of three. Simulations by Wada et al. (2018) suggest that the apparent power-law dependence of X_{CO} on I_{CO} may be even steeper than that put forth in Paper IV. These proposed power-law alternatives to the X_{CO} factor may reduce the need for so-called CO-dark gas in the diffuse

envelopes of molecular clouds (MCs), where H_2 is dense enough to self-shield but CO has been photodissociated (Blitz et al. 1990; Reach et al. 1994). For instance, the GOTC+ team, who used the standard X_{CO} factor to calculate molecular gas masses from CO observations, suggests that CO-dark percentages may vary from ~20% for dense, massive clumps to ~70% for diffuse H_2 filaments (Pineda et al. 2013; Langer et al. 2014). If the method of Paper IV or the fit presented in Section 3.3 proves more appropriate, the fraction of H_2 in CO-dark gas in dense clump settings may be less significant, given typical uncertainties in total clump mass of ~20%.

In this article, we expand on the results of PBV19 to show that absolute CO abundance variations are widespread in massive molecular gas clumps and correlate strongly with T_d in Section 3.1. We present a set of best-fit parameterizations for these effects in Section 3.2, which we recommend for future studies of dense molecular clumps. Further, via comparison of N_{H_2} derived from dust continuum observations to $I_{^{12}CO}$, we reveal in Section 3.3 among the strongest evidence to date that the X_{CO} factor is systematically dependent on the density (ergo shielding) and excitation conditions of the gas. We conclude with some of the implications of these findings in Section 4.

2. Data and Methods

2.1. CO

The 2009–2012 phase of Mopra telescope observations for the CHaMP project (Stage II) mapped the ^{12}CO, ^{13}CO, C^{18}O, and other line data across for the brightest 267 prestellar clumps detected in HCO$^+$ in Stage I (see Paper I; Paper I–B; Paper III–B, for Phase I data). For the Stage II analysis, integrated ^{12}CO line intensities (denoted $I_{^{12}CO}$) and CO column densities (denoted N_{CO}) were derived by performing full radiative transfer on all three isotopologues, assuming typical Galactic isotopic ratios. Paper III discusses the Stage II observing plan and conditions, reduction techniques, and radiative transfer equations in great detail.

2.2. Dust Continuum

We stacked archival far-infrared (FIR) and submillimeter data from 70 to 870 μm, with optional data for a second component from 3.4 to 24 μm, and fit pixel-by-pixel color-corrected modified Planck SEDs using the IDL code built around MPFIT (Markwardt 2009). We used data from Herschel-PACS (Poglitsch et al. 2010), Herschel-SPIRE (Griffin et al. 2010), APEX-LABOCA (Siringo et al. 2009), and, where helpful to separate out warmer temperature components, WISE (Wright et al. 2010) and MIPS-24 μm (Rieke et al. 2004), all obtained from the Infra-Red Science Archive (IRSA). Our anonymous code package is publicly available[6] and it includes several model options and color correction functionality. We assume a gas-to-dust ratio γ of 100, dust emissivity index β of 1.8, and opacity of κ_0 of 0.55 m^2 kg^{-1} at 250 μm as per the results of the Planck Collaboration's studies of the Galactic plane (see, e.g., Planck Collaboration et al. 2011). Because of the CHaMP sample's proximity to the Carina tangent, we assume negligible foreground and background components except in the cases of Regions 23 and 26, which lie in front of the Dragonfish Nebula. We also do *not* assume optically thin dust emission

---

[6] https://github.com/rlpitts/Mosaic-Math

Table 1
Sky Coverage and Some Contents of Each Region (see also Paper I, Figure 2)

Region	ℓ Range (deg)	b Range (deg)	BYF Clumps	Noted Objects in Region
1	280°69 to 281°55	−1°87 to −0°95	2–5, 7–9	IRAS 09578−5649[a]
2a	281°48 to 281°78	−1°17 to −0°49	10, 12–14, 16	MMB G281.710-01.104[b]
2b+3	281°65 to 282°32	−2°10 to −1°35	15, 18–22, 25, 26	RAFGL 4101[c]
2 c	282°16 to 282°35	−0°92 to −0°41	23, 24, 27	THA 35-II-3[d]
5	282°78 to 283°25	−1°07 to −0°92	32, 36, 37	IRAS 10123−5727[a]
6	283°96 to 284°21	−1°11 to −0°76	40–42	SEST 39[e]
7	284°64 to 284°72	−0°71 to −0°53	47	…
8	284°79 to 285°43	−0°16 to +0°18	50, 54, 56	Hoffleit 18[f]
9	286°00 to 286°46	−0°45 to +0°24	63, 66–73, 76–79	Gum 31, NGC 3324 (CNC)
10	286°90 to 287°54	−0°99 to −0°05	85–104	Tr14, Northern Cloud (CNC)
11	287°61 to 288°31	−1°25 to −0°42	105–118	Southern Cloud/Pillar (CNC)
12	291°28 to 291°53	−1°79 to −1°59	127, 130	…
13	291°19 to 291°70	−0°81 to −0°16	126, 128, 129, 131, 132	NGC 3576, NGC 3603
15	291°97 to 292°05	−2°00 to −1°92	134	…
16	293°01 to 293°38	−1°08 to −0°74	141, 142, 144	Bran 354A[h]
18	293°62 to 293°84	−1°77 to −1°59	149, 150	Bran 362B[h]
21	294°76 to 295°23	−1°84 to −1°54	161–163, 165, 167	IC 2944/2948
23	298°14 to 298°48	+0°65 to +0°80	185, 190	IRAS 12091−6129[i]
26a	298°86 to 298°94	+0°31 to +0°50	199	…
26b	298°94 to 299°58	−0°48 to −0°17	201–203, 208	RCW 64[j], Bran 386B–G[h]

Notes.
References. [a] Olnon et al. (1986). [b] Green et al. (2012). [c] Grasdalen et al. (1983). [d] The (1966). [e] Harju et al. (1998). [f] Hoffleit (1953). [g] Gum (1955). [h] Brand (1986). [i] Walsh et al. (1997). [j] Rodgers et al. (1960).

because there was no significant computational benefit to doing so, and we find that optical depths near 70 μm can approach 1. We refer readers to PBV19 for a complete description of the SED-fitting routine and its features.

2.3. Objects Covered

The CHaMP survey target fields are divided into 27 regions with multiple prestellar clumps, plus a number of isolated prestellar clumps, that were mapped by NANTEN2. Of these, 18 regions and one isolated clump (BYF 123) had complete or nearly complete coverage by both Herschel and Mopra. We initially tested the pixel-by-pixel SED-fitting pipeline on Regions 9 and 26 (in and around Gum 31 and RCW 64, respectively) and then expanded our analysis to Regions 10 and 11 (the northern and southern halves of the Carina Nebula Complex, respectively) to complete PBV19. In the following sections, we expand our sample to cover CHaMP Regions 1–3, 5–8, 12 (marginal), 13, 16, 18, 21, and 23. Table 1 summarizes the contents and sky coverage of each region.

3. Results and Discussion

3.1. Temperature, Density, and Morphological Trends in the Full CHaMP Sample

Figure 1 shows a sample set of dust temperature and H_2 column density maps, as well as their uncertainty maps, for Region 13. Dust temperature, H_2 column density, and CO abundance maps by region, for all regions not covered in PBV19, are included in online-only figure sets associated with Figures 1 and 6, respectively. Most of Region 13 is unusually warm, but we chose it as the example because it shows the greatest diversity of physical conditions across a region.

Most clumps in Figure 2 and the associated online-only figure set show T_d declining, in a variety of functional forms, as N_{H_2} increases. This broadly inverse relation between temperature and column density is the opposite of the trend one typically observes for N_{H_2} and T_{ex} for CO (e.g., Kong et al. 2015; Gong et al. 2018), but it is to be expected if molecular line emission, particularly from CO, is the predominant coolant in MCs. Even clumps that are known to contain or border on active star-forming regions—like BYF 40b, 109a, 150, and 203 —sometimes still show higher T_d at lower column densities. Some particularly warm comet-shaped clumps, like BYF 103a, form a slightly concave-up curve in T_d–N_{H_2} space suggestive of a compressive front. Not every cometary globule has this shape in the plot of T_d versus N_{CO}, but every clump that has this functional form is a cometary globule.

Overall, at least 84% of prestellar clumps in the CHaMP survey that could be separated in dust continuum emission showed clear anticorrelations between T_d and N_{H_2} (see Figure 2–3), with many of the others too small to judge accurately. We checked for this trend by evaluating the trend in T_d versus N_{H_2} over 2σ in both the major and minor axes around each clump and calculating the Spearman rank correlation coefficient. We used the Spearman rank correlation coefficient rather than the Pearson correlation coefficient because the latter assumes a linear relationship between parameters, whereas the former only demands that a correlation be monotonic. The 16% of clumps that had flat or positive Spearman coefficients of correlation between T_d and N_{H_2} were systematically warmer at the location of the peak in N_{H_2} but were not all associated with other signs of star formation. Some, like BYF 103a and b (see online-only version of Figure 2, ninth figure in the set), were simply not monotonic. The clumps known to be associated with other indicators of star formation, like masers and Two Micron All Sky Survey (2MASS) embedded cluster candidates, showed large scatter in their T_d versus N_{H_2} plots and typically (though not always) had Spearman coefficients $>+0.25$. One known clump around a protocluster, BYF 73, still had a negative Spearman coefficient,
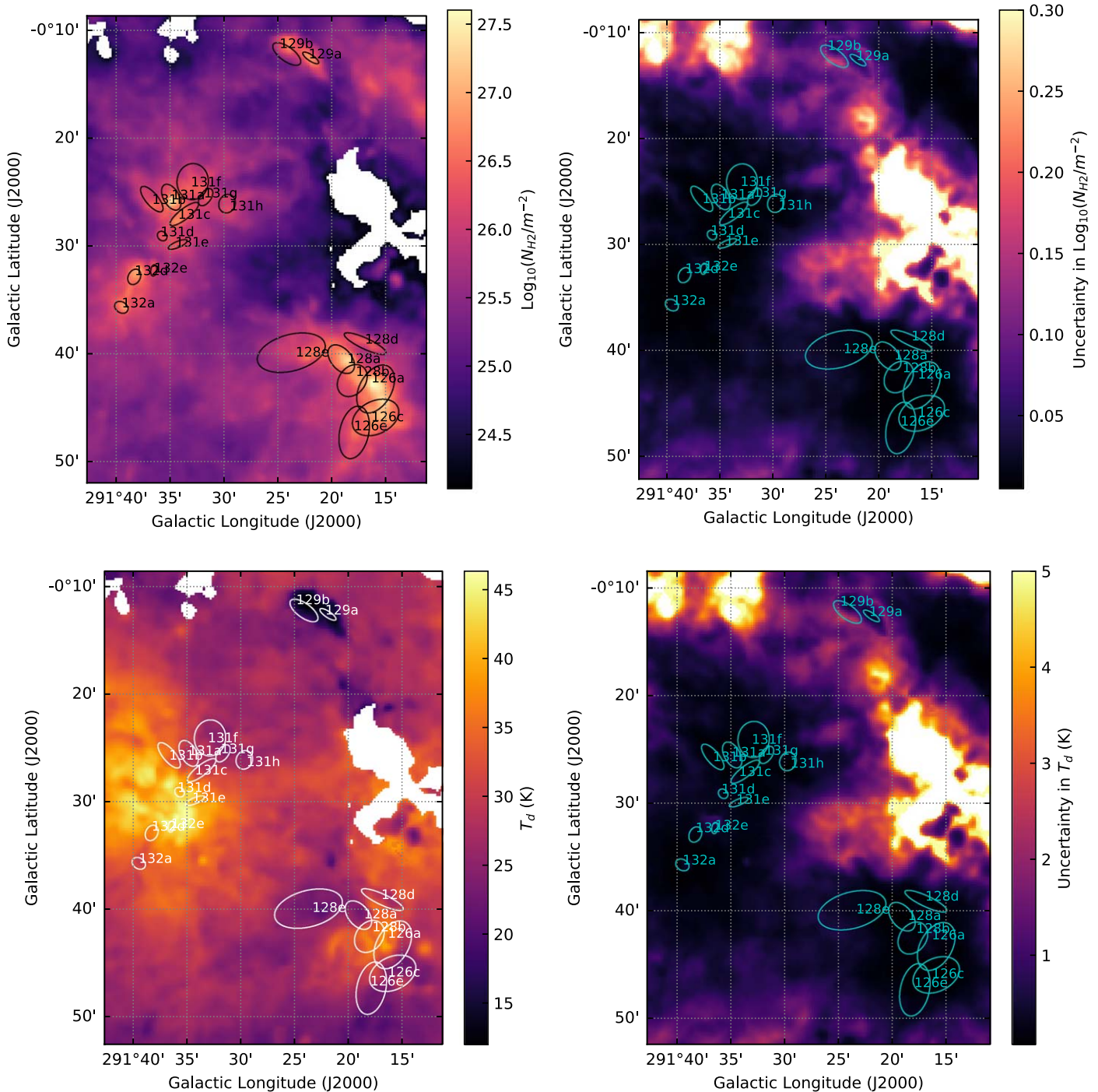
Figure 1. SED-fitting parameter maps for Region 13. Top row: N_{H_2} (left) and N_{H_2} uncertainty (right) maps. Bottom row: T_d (left) and T_d uncertainty (right) maps. The complete figure set (26 images for N_{H_2} and T_d maps of each region) is available in the online journal.

(The complete figure set (26 images) is available.)

but as shown in Pitts et al. (2018), this clump is some 98% gas dominated. The Spearman correlation coefficient between N_{H_2} and T_d may only be sensitive to star formation at a somewhat later stage and will be dependent on spatial resolution.

These results are generally consistent with prestellar molecular clumps being long-lived structures as previously evinced in Barnes et al. (2018). Specifically, it suggests that clumps without a strong internal heat source ("prestellar," or more ambitiously, "starless") last ∼10 times as long as clumps

exhibiting active star formation (Figure 3). In other words, most of the gas-phase evolution of a clump happens in the last ∼10% of its lifetime. This also makes sense in light of simulations showing that the cooling efficiency of CO increases with temperature and density (Juvela et al. 2001; Stahler & Palla 2005; Gong et al. 2018): purely gas-dynamical changes in temperature and pressure should be damped. However, this damping of effects also means that a clump can contain extremely young protostellar cores while still appearing cold
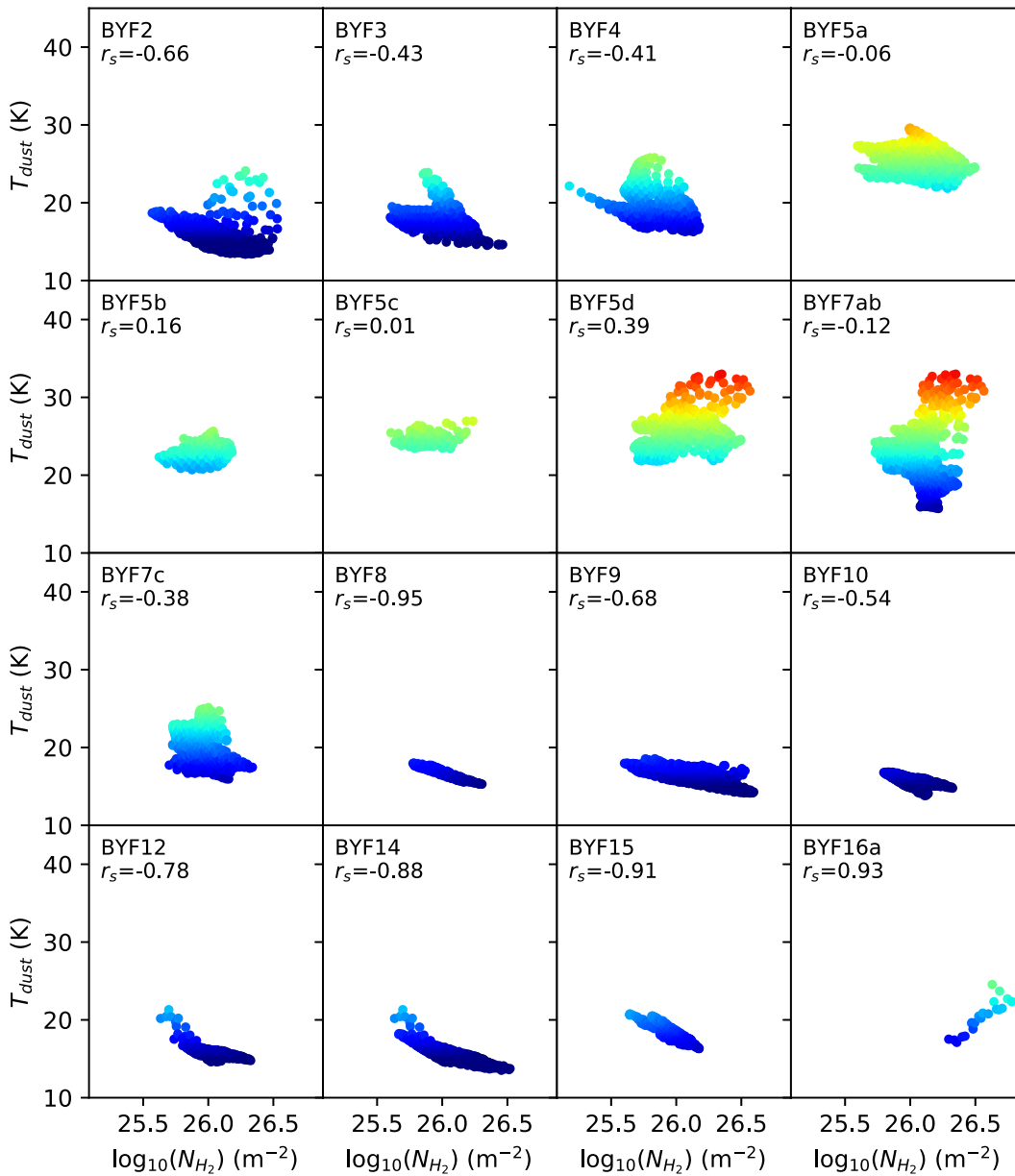
Figure 2. T_d vs. N_{H_2} plots for clumps in Regions 1 and 2a. Spearman rank correlation coefficients (r_s) are given under the BYF catalog numbers. The complete figure set (16 images for all clumps) is available in the online journal. The online figure set includes T_d vs. N_{H_2} for the pixels in each clump, masked to the CO-emitting area as defined in Paper III and also colored by T_d. For completeness, the online figure set includes region-wide plots, masked to all pixels mapped in CO, with translucent points to make coherent structures stand out.

(The complete figure set (16 images) is available.)

and CO depleted at clump scales. Indeed, our group wrote about the protostellar content of BYF73 in Pitts et al. (2018) while documenting its clump-scale appearance of CO depletion and lower-than-ambient temperatures in PBV19, Figures 6 and 11. Thus, observational applications of these models to verify a clump's evolutionary state demand detailed accounting of heating mechanisms, like embedded protostars. This means that catalog matching would have to be done in search of star formation indicators within each clump's angular area–e.g., astrophysical masers, outflows, or K-band point sources. Besides BYF73, we have done this manually where hot spots and hollows in the column density maps were immediately apparent (see Table 2), but follow-up on other sources is ongoing.

The CHaMP clumps (again ∼1 pc in size) are more than 10 times farther away and sample a much greater diversity of environmental conditions than the cold dense cores (∼0.1 pc) in the Pipe Nebula studied by Hasenberger et al. (2018), but that study is a potentially useful point of comparison. For more direct comparison, we converted N_{H_2} to an optical depth at 850 μm and fit each clump with a line in log[T_d]–log[τ(850 μm)] space (a power law in linear space), with τ(850 μm) multiplied by 10^4. The resulting distribution of power-law exponents, shown as a histogram in Figure 4, was more symmetric and less purely negative than the distribution of the same parameter in Hasenberger et al. (2018). The power-law exponents for the CHaMP clumps ranged from about −15 to +5 with a mean of about −4, compared to typical values between −5 and −10 and
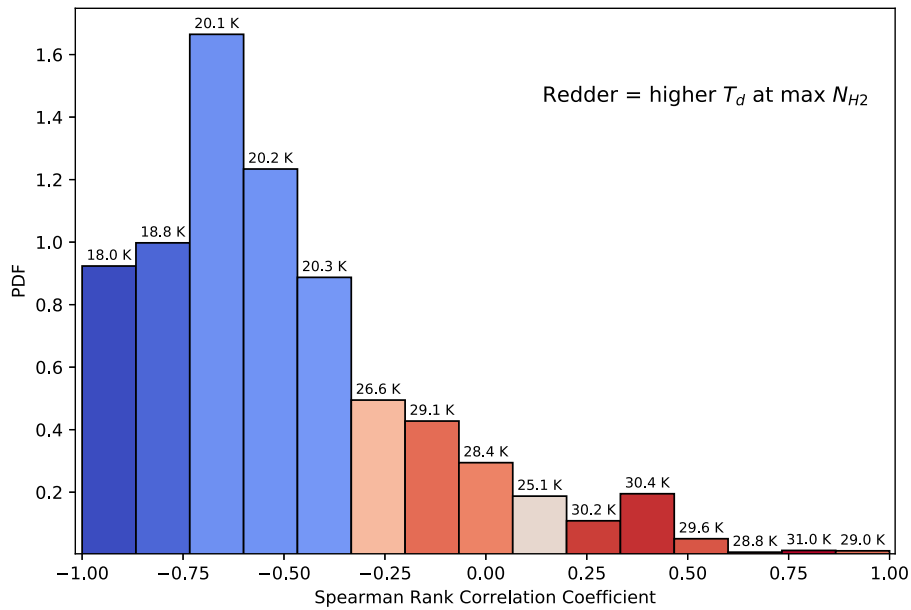
Figure 3. Histogram probability distribution function (PDF) of Spearman rank coefficients of correlation between T_d and N_{H_2}. The Spearman coefficients themselves correlate with a clump's T_d at the position of maximum N_{H_2} (indicated by the coloration of the bins, where redder bins have higher T_d.)

a range of -40 to 0 in Hasenberger et al. (2018). Besides the inclusion of actively star-forming clumps, we suspect that at least some of the difference is down to resolution for reasons that should become clearer when we discuss the morphotype scheme developed in PBV19. We also see much more substructure in the plots of temperature versus density (or optical depth), at least some of which must be due to how we defined the boundaries of the clumps. Where Hasenberger et al. (2018) worked directly with local minima identified in T_d maps, the CHaMP clumps are defined by CO emission. As shown in PBV19 and in the appendices, CO tends to be underabundant in the coldest density enhancements, so multiple local N_{H_2} maxima sharing a common envelope can look like a single structure in CO. For a truer, apples-to-apples comparison with the physical conditions inside the Pipe Nebula cores, the CHaMP sample would have to be redefined using, e.g., an algorithm like Clumpfind (Williams et al. 1994) directly on the N_{H_2} maps.

In general, we find that the morphotype scheme defined in PBV19 continues to be a relevant aid in describing and understanding the spatial variation of CO abundance, both across individual clumps and across their larger regions. To review, we classified prestellar clumps into five major groups depending on the relative positions or geometries of N_{H_2} maxima and CO abundance extrema:

1. Coincident- or C-Type if N_{H_2} and the CO abundance both peaked in the same location, or if the CO abundance appeared constant across the clump.
2. Asymmetric- or A-Type if there was a CO abundance maximum within the clump boundaries as defined in Paper III, but it was noticeably offset from the N_{H_2} maximum.
3. Frozen-out- or F-Type if the N_{H_2} maximum coincided with a local minimum in CO abundance surrounded by a ring or filament of enhanced CO abundance.
4. FA-Type if the N_{H_2} maximum coincides with a CO abundance minimum that is only partly bounded by enhanced CO abundance.

5. Peculiar- or P-Type in the rare case that there is no visible N_{H_2} enhancement at the location of a clump defined by CO emission.

In many cases, it was possible to further classify A- and FA-Type clumps into sublimating (s(F)A-Type) or dissociating (d (F)A-Type) subtypes based on the projected positions of nearby far-UV (FUV) sources relative to the N_{H_2} maxima and CO abundance enhancements surrounding zones of depletion. Clumps classified as sA- or sFA-Type had CO abundance enhancements along the side facing the FUV sources, and clumps classed as dA- or dFA-Type had any proximal CO enhancements behind the N_{H_2} maximum relative to the FUV source. Figure 5 (adapted from PBV19) qualitatively illustrates the appearances of all the types and subtypes in the CO abundance maps.[7] As discussed at great length in PBV19, a prestellar clump's morphotype also generally correlates with its minimum temperature. F- and FA-Types systematically reached cooler temperatures than C- or A-Types and more consistently displayed a clear anticorrelation of T_d with N_{H_2}.

The abundance map of Region 13 shown in Figure 6 provides a helpful demonstration of the various abundance morphotypes all in one image owing to the proximity of several prestellar clump groups in varying stages of development. CO abundance maps for the remaining regions can be found in the online-only version of Figure 6. Each of the three clusters of clumps in Region 13 is a product of a different environment viewed at a different distance. BYF 129 (top), by far the closest at about 1.2 kpc away (Barnes et al. 2011, and references therein), is an extreme example of an F-Type: cold ($\sim$12 K) and strongly depleted. A quick look at the interactive three-color 2MASS image on SIMBAD shows that BYF 129 is an infrared dark cloud. The various components of BYF 126 and 128, both about 2.4 kpc away, trace a dense filament cutting across the (Galactic) southwest of NGC 3576 that appears to be CO

---

[7] "Undisturbed" is probably a bit of a misnomer, since the geometries of A- and FA-Type clumps are likely attributable to external irradiation more often than not. The circle on the left more accurately shows how the clumps appear, and are categorized, before assessing the influence of environment.

Table 2
Identified Hot Spots and Other SF Tracers within CHaMP Clumps

| BYF No.	Hot Spot ID(s)	Masers	SiO (Outflows)	MIR (5–25 μm)	NIR (0.7–5 μm)	H I and Hα	H II	X-Rays
2	IRAS 09568–5619	...	...	+[a]	[aa]	...	?[a]	...
3	IRAS 09581–5607	...	...	+[b c]	...	...	...	...
5a[ab]	IRAS 09572–5636	...	...	+[b]	...	...	...	...
5d	MSX6C G281.0472-01.5432	...	...	+[d e]	[aa]	...	...	...
7ab	DBSB 125/IRAS 09578–5649	...	...	... +[a f]	+[g]	...	?[a]	...
9	2MASS J10001718–5720342	...	...	+[d e]	+[h]	...	...	...
11a	IRAS 09563–5743	...	...	+[a]	+[i]	...	+[i a]	...
16a	MMB G281.710-01.104, 2MASS J10050568–5657023?	CH$_3$OH[j]	...	+[a d e]	+[h]	...	?[a]	...
27	THA 35-II-3/PDS 37	...	...	+[d e]	+[h]	+[k l m]	...	...
36 c	IRAS 10123–5727	...	...	+[f]	...	...	...	...
36d	AllWISE J101417.36-574316.4	...	...	+[n]	[aa]	...	...	...
40a	GAL 284.0-00.8/SEST 39	CH$_3$OH?[o]	+[o]	+[a b d e]	...	...	?[a]	...
54a	Caswell OH 285.26-00.05, DBSB 48, GAL 285.3-00.0 IRAS 10295–5746	CH$_3$OH[p], H$_2$O[q], OH[r]	[o]	+[a f],	+[g h]	+[s]	+[s] ?[a]	...
56a	IRAS 10303–5746, MMB G285.337-00.002?	CH$_3$OH[j t]	...	+[a b]	...	...	?[a]	...
73	DBSB 127, SEST 44	H$_2$O[u]	+[o]	+[a d e v]	+[g h]	+[v]	?[a]	...
77 c	MSX6C G286.3773-00.2563, IRAS 10361–5830? CXOU J103801.8–584642?	...	...	+[d v]	+[h]	+[v]	+[v]	?[w]
103a	2MASS J10445816–5931166, XMMU J104458.4–593115	...	...	+[x]	+[h x]	...	...	+[y]
109a	Treasure Chest Cluster	...	...	+[z]	+[g A B]	+[B C]	...	+[D]
115a	2MASS J10481308–5958516	...	...	+[x]	+[h x]	...	...	...
126a	2MASS J11115198–6118374, SEST 47	H$_2$O[p]	+[o]	+[d e]	+[h E]	...	...	...
131a	Caswell OH 291.57-00.43, SEST 49	CH$_3$OH[F], H$_2$O[q], OH[r]	+[o]	+[c G H]	+[H]	?[H]	...	?[I]
163a	MSX5C G294.9709-01.7271, RAFGL 4134	CH$_3$OH[J], H$_2$O[K]	+[o]	+[G]	[aa]	...	(in IC2948)	?[L]
163b	MMB G294.990-01.719, La Serena 2?	CH$_3$OH[j]	...	+[M]	+[M]	...	(in IC2948)	?[L]
185	IRAS 12091–6129	CH$_3$OH[N]	...	+[G O]	+[P]	...	?[N]	...
190b[ab]	Bran 382/GN 12.10.3, IRAS 12102–6133	...	...	+[b M Q]	+[M R]	...	...	...
203a	IRAS 12175–6236, VVV CL012	...	...	+[b M]	+[S]	...	...	...
203d[ab]	Bran 386E/RCW 64 La Serena 31?	...	...	+[Q] ?[M]	+[R] ?[M]	+[T]	+[T]	...

Notes. Table note marks for each detection correspond to the following references.

References. [aa] Hot spot is in clump CO-emitting area but not coincident with a local N_{H_2} maximum. [ab] Object is visible in images in this wavelength range but has no catalog ID in the respective survey. [a] Bronfman et al. (1996). [b] Helou & Walker (1988). [c] Cutri et al. (2012). [d] Egan et al. (2003). [e] Mottram et al. (2007). [f] Olnon et al. (1986). [g] Dutra et al. (2003). [h] Cutri et al. (2003). [i] Giveon et al. (2002). [j] Green et al. (2012). [k] Wray (1966). [l] The (1966). [m] Gregorio-Hetem et al. (1992). [n] Cutri et al. (2013). [o] Harju et al. (1998). [p] Batchelor et al. (1980). [q] Caswell & Haynes (1987). [r] Wilson et al. (1970). [s] Braz & Epchtein (1983). [t] van der Walt et al. (1995). [u] Scalise et al. (1989). [v] Cappa et al. (2008). [w] Preibisch et al. (2014). [x] Povich et al. (2011). [y] Albacete Colombo et al. (2003). [z] Rathborne et al. (2004). [A] Dutra & Bica (2001). [B] Smith et al. (2005). [C] Smith et al. (2010). [D] Feigelson et al. (2011). [E] Maercker et al. (2006). [F] Caswell (2004). [G] Egan et al. (2003). [H] Nürnberger & Stanke (2003). [I] Sung & Bessell (2004). [J] Schutte et al. (1993). [K] Braz et al. (1989). [L] Nazé et al. (2013). [M] Barbá et al. (2015). [N] Walsh et al. (1997). [O] Cyganowski et al. (2008). [P] Ishihara et al. (2010). [Q] Simpson et al. (2012). [R] Brand (1986). [S] Borissova et al. (2011). [T] Rodgers et al. (1960).

depleted toward the middle and enhanced on the ends. The minima in BYF 128a and 126 c may not be the most depleted clumps in the filament: BYF 128b and 126a cover a patch of saturated emission at 250 μm, so T_d and N_{H_2} for these two clumps are highly uncertain. The most distant groupings at over 6 kpc away, BYF 131 and 132, surround the massive cluster NGC 3603. BYF 131d and g are C-Types, and the rest (where enough data exist to classify them) are A-Types, mostly of the dissociating subtype. Due to their distance, it is reasonable to suspect that the C-Type clumps in the BYF 131 and 132 groups might have a very different classification if viewed at a different angle or closer distance.

This system is not scale-free, and the temperature segregation is less clean than it initially appeared. Small F- and FA-Type clumps viewed at sufficient distance may look like C- and A-Type clumps, respectively, which may in part explain why many more of the latter types were identified with lower temperatures. Two clumps originally designated as F-Type were found to be warmer rather than colder toward their dense centers. These were readily identified as known protostellar
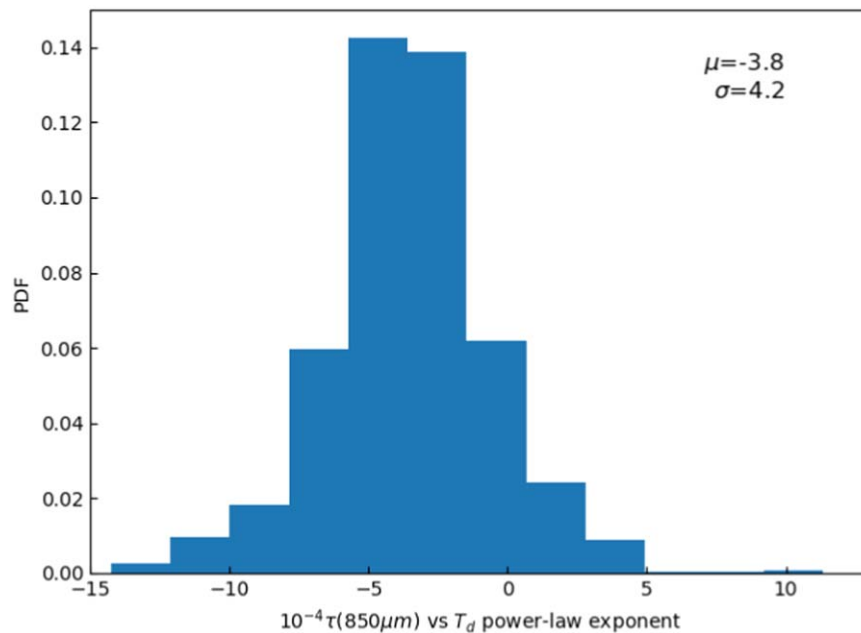
Figure 4. Histogram PDF of power-law exponents for the fits of optical depth $\tau(870\ \mu m)$ vs. T_d. This was done strictly for comparison with the work of Hasenberger et al. (2018).
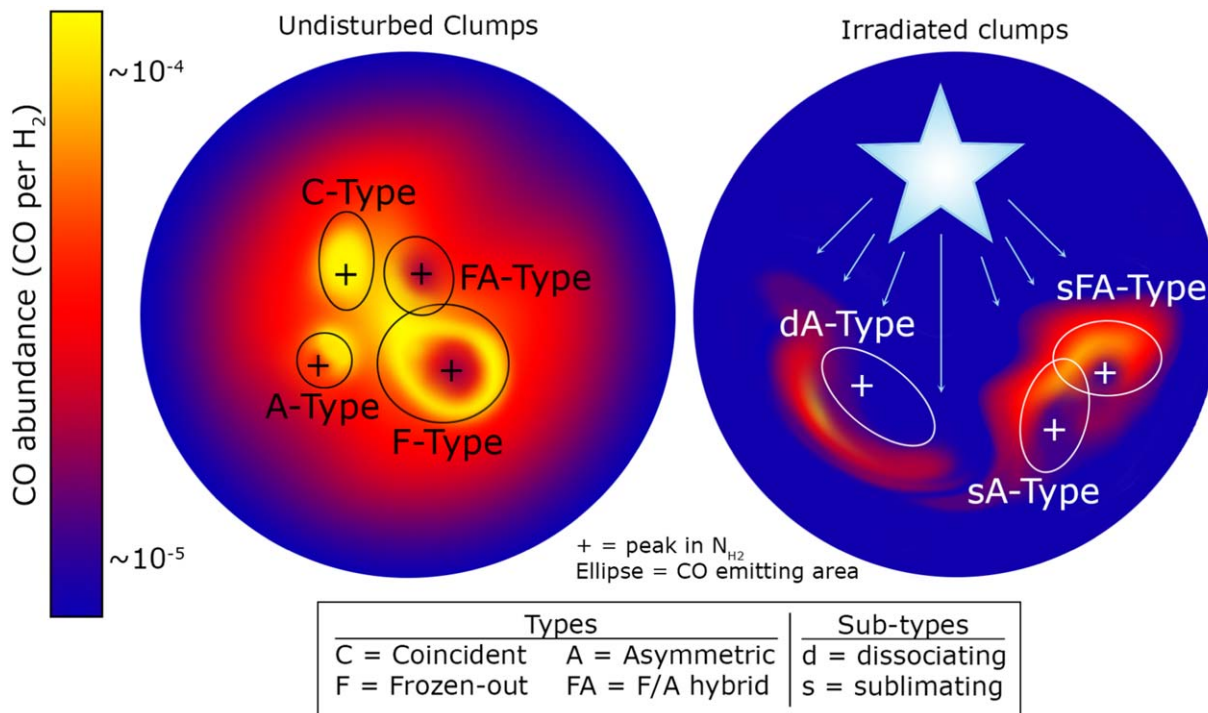

Figure 5. Illustration, adapted from PBV19, of the clump morphotype scheme defined therein. Mathematical values are only approximate.

objects with associated masers and outflows on SIMBAD. Aside from them, the range of temperatures seen in F- and FA-Types did not increase like it did for the other morphotypes, despite a similar increase in the total number of clumps of these two types. This is somewhat unexpected given that the range distances probed by the CHaMP survey on average account for less of the variation in size than intrinsic differences in the source dimensions. It was probably just luck given that several more clumps initially identified as FA-Types were also found

to be associated with embedded objects after inspecting them in the T_d maps.

Besides requiring adequate separation of clumps, the morphotype classification scheme originally assumed that any CO line emission structure fully enclosing a compact H II region would be broken up into two or more clumps by virtue of the kinematics or temperature effects. That held true for Regions 9–11 and 26, but between Regions 1–3, 6, 8, and 13, we noted a handful of clumps where that assumption breaks
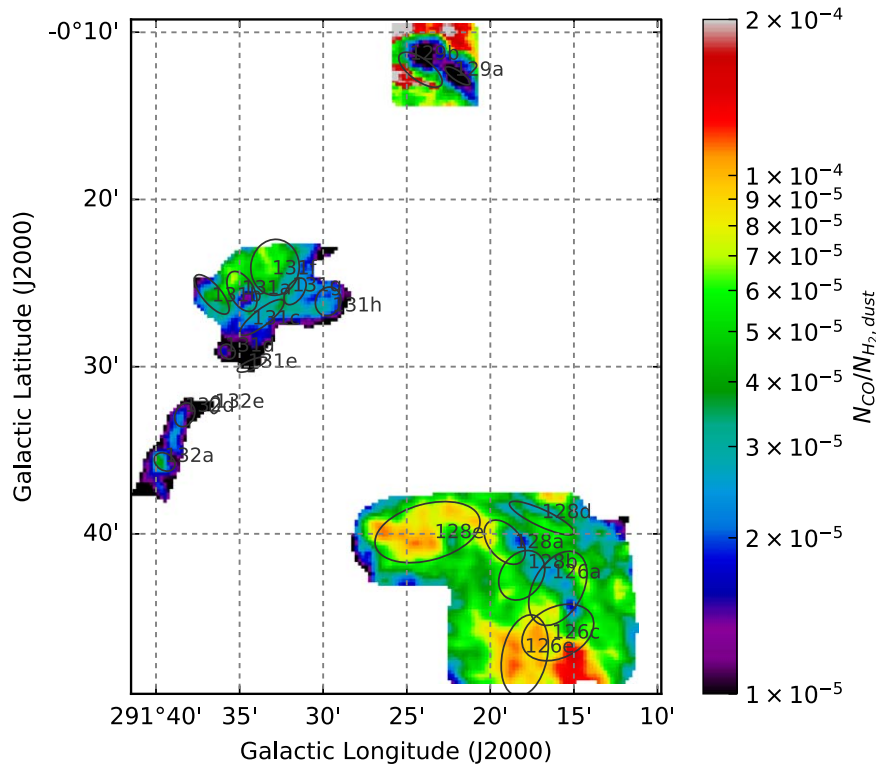
Figure 6. [N_{CO}/N_{H_2}] map for Region 13, shown as an example. The complete figure set (17 images) is available in the online journal.
(The complete figure set (17 images) is available.)

down: BYF 5d, 7ab, 16a, 19b, 27, 40a, 54a, 56a, and 131a. Notably, every one of these clumps appears coincident with one or more known embedded sources, UCHII regions, or astrophysical masers within the clump's CO-emitting area defined in Paper III, as we found on SIMBAD and summarized in Table 2. The two misclassified F-Types, BYF 16a and 27, also happened to be the only two of these warm clumps with minimum temperatures exceeding 25 K. Table 2 lists the clumps containing identified hot spots, the best-known sources therein, and a checklist of star formation tracers detected. Only the reference for the first detection that is not an upper limit is listed if the same source is observed multiple times in the same tracer. Indirect or otherwise-unconfirmed detections are indicated with a question mark after the citation.

BYF 16a, 19b, 40a, 54a, and 131a all have coincident T_d and N_{H_2} maxima, and all are associated with at least one maser. BYF 56a also shows maser activity but still met all the criteria for an A-Type clump. BYF 27 is centered on the Herbig Be star THA 35-II-3 (The 1966), and the two objects' distances are well within each other's margins of error (Ababakr et al. 2015; Yonekura et al. 2005). Both BYF 7ab and 40a would have been designated A-Types, but after accounting for the multiple temperature extrema within each, the published dimensions of these two objects may warrant revision. In addition to the above, BYF 2 and 3 also contained a handful of tiny hot spots, but these were not associated with N_{H_2} maxima, nor did they seem to substantially affect their clumps' CO abundance distributions. Given these observations, and the fact that BYF 2 and 3 are among the closest clumps to the Carina Tangent, they may be background sources or may simply have not been

bright enough in NANTEN observations to make the cut for Mopra follow-up observations.

3.2. Temperature and CO Abundance

Useful as the morphotype scheme is, one of the real strengths of the full CHaMP sample is that the number of pixels and the variety of environments are sufficient to start quantifying the correlation between T_d and [N_{CO}/N_{H_2}] directly, for the first time outside of the laboratory. Plotted as a two-dimensional histogram, the fragments first shown in Figure 18 of Pitts et al. (2019) merge into the distinct concave-down trend shown in Figure 7(a). Figure 7(a) is the Gaussian-kernel-density-smoothed distribution of the CO abundance versus dust temperature in log–log space, which we fit empirically with a parabola in $\log T_d$ so that the parameters of the fit could be sanity-checked by eye. Kernel density smoothing was required to make the fit converge at the highest density of points. The residuals of the fit are shown in panel (b), with the 1σ dispersion marked by red dashed lines. Higher-order polynomials did not improve the fit near the limits of the temperature range that our data probe. For brevity, hereafter we use ϱ to denote the *fitted* [N_{CO}/N_{H_2}] ratio as a function of T_d, which has the form

$$\log_{10} \varrho = \log_{10}\left[\frac{N_{CO}}{N_{H_2}^{dust}}\right] = 0.25 f^{-1} \log_{10}^2$$
$$\times \left(\frac{T_d}{T_{d,0}}\right) + \log_{10} \varrho_0 \qquad (1)$$
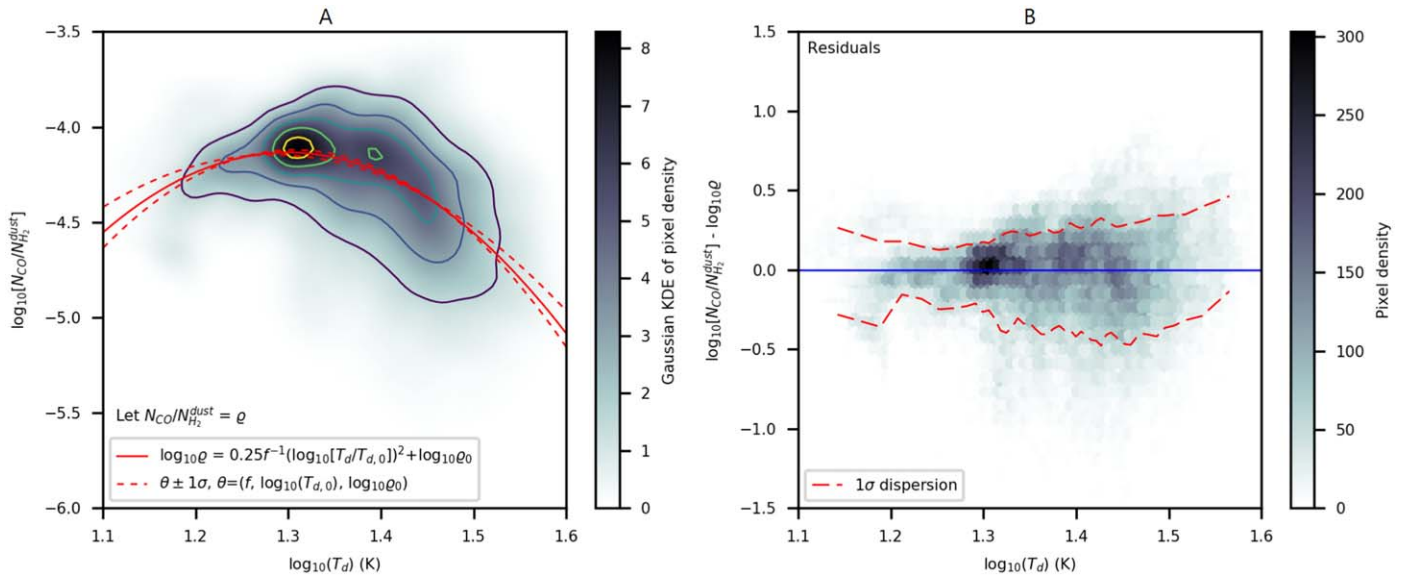
Figure 7. Log–log plot of $[N_{CO}/N_{H_2}]$ vs. T_d, with fitted curve and residuals. (a) Gaussian-kernel-smoothed pixel density plot of CO abundance (denoted ϱ) vs. T_d, fitted empirically with a second-degree polynomial in log-space (red solid line). The dashed red lines show fits where the parameters are adjusted by 1σ in their mutual posterior probability distributions as estimated by MCMC. (b) Pixel density distribution of residuals in the fit of ϱ vs. T_d, with the 1σ dispersion around the binned average indicated by red dashed lines.

in the log. The coefficients f, $\log_{10} T_{d,0}$, and $\log_{10} \varrho_0$, respectively, represent the focus of the parabola, the log of the T_d where $[N_{CO}/N_{H_2}]$ is maximized, and the log of the maximal $[N_{CO}/N_{H_2}]$ ratio. We find that $0.25f^{-1} = -10.0^{+0.8}_{-2.4}$, $\log_{10} T_{d,0} = 1.30^{+0.01}_{-0.02}$ K ($T_{d,0} = 20.0^{+0.4}_{-1.0}$ K), and $\log_{10} \varrho_0 = -4.13^{+0.01}_{-0.02}$ ($\rho_0 = 7.4^{+0.2}_{-0.3} \times 10^{-5}$ per H_2).

Since we fitted a kernel-smoothed resampling of the data rather than the data themselves, simple curve-fitting routines did not provide usable error estimates. The best way to estimate the uncertainty was to minimize a negative log-likelihood function and use the Python MCMC package `emcee` (Foreman-Mackey et al. 2013) to estimate the posterior distributions of f (the parabolic focus, with unclear physical significance), $\log_{10} T_{d,0}$, and $\log_{10} \varrho_0$. A Gaussian noise term, ϵ, was also included as a stand-in for unquantified factors expected to influence the dispersion of the data, chief among them the local interstellar radiation field (ISRF). However, the fitted value was 10^{-12}, so it was removed with no effect on the other parameters. The posterior distributions are plotted in Figure 8. We used uniform priors with the following loose restrictions based on what was apparent from the plot: $-10 < f < 0.0$, $0.5 < \log_{10} T_{d,0} < 2.0$ (that is, $T_{d,0}$ must be between 3 and 100 K), and $-10.0 < \log_{10} \varrho_0 < 0.0$. The log-likelihood function used assumes that the posterior distributions are close enough to Gaussian that the estimated closed form of the likelihood function for a skew-normal distribution would not have offered a significant improvement. The dispersion in CO abundance as a function of T_d is about 0.3 dex over most of the data, with the smallest dispersion between about 15 and 20 K and the largest between 25 and 30 K.

To be clear, Equation (1) is a purely empirical model intended for observational astronomers with large data sets and limited need to delve into astrochemistry. The benefit of this approach lies in the simplicity of the method: the model is sufficiently simple and geometric that, provided that there are enough data on the plot to form a coherent structure (we find

that the trend requires at least half of all the CHaMP data or a few $\times 10^4$ pixels to see easily), the parameters of the fit can be estimated to within a factor of a few by eye for easy initialization. The most obvious missing piece right now is the strength of photodissociating interstellar radiation, the FUV part of the ISRF. The greatest region-to-region variability is almost always in the high-temperature side of the distribution, where trends for smaller individual regions suggest that the relative symmetry with the low-temperature side may be due to averaging over many much steeper trends.

One popular method of estimating the FUV field strength from FIR/submillimeter data is to follow Kramer et al. (1999) in assuming that nearly all FIR emission is reprocessed FUV emission, and so the ISRF is proportional to the integral of the SED. There are two problems with this approach as it pertains to our study. First, it assumes that internal heating is negligible —not a terrible assumption when close to 90% of prestellar clumps are effectively quiescent (at this resolution) and as likely to be dispersing as accreting (Barnes et al. 2018)—but where that assumption fails, the internally heated gas falls in the part of the $[N_{CO}/N_{H_2}]$–T_d plot where the ISRF is most needed to explain the dispersion. Second and more importantly, much like L/M (see discussion in PBV19, Section 4.2), the ISRF field computed this way is not an independent quantity. All of the variables used to compute it are already in Equation (1) in some form.

Comparison of this temperature–abundance distribution to laboratory measures of ion current through CO (proportional to the partial pressure or column density of CO in the gas phase) versus substrate temperature reveals several possible features of astrophysical interest. First, as detailed previously in Pitts et al. (2019), laboratory experiments show that the amount of gas-phase CO peaks for substrate temperatures between 27 and 30 K in the absence of an externally applied UV field (Öberg et al. 2009; Muñoz Caro et al. 2010, 2016; Noble et al. 2012). As one might expect for a range of environments with nontrivial ISRFs, in Figure 7, the peak abundance in CO occurs at a substantially lower temperature, $20.0^{+0.4}_{-0.9}$ K. A value
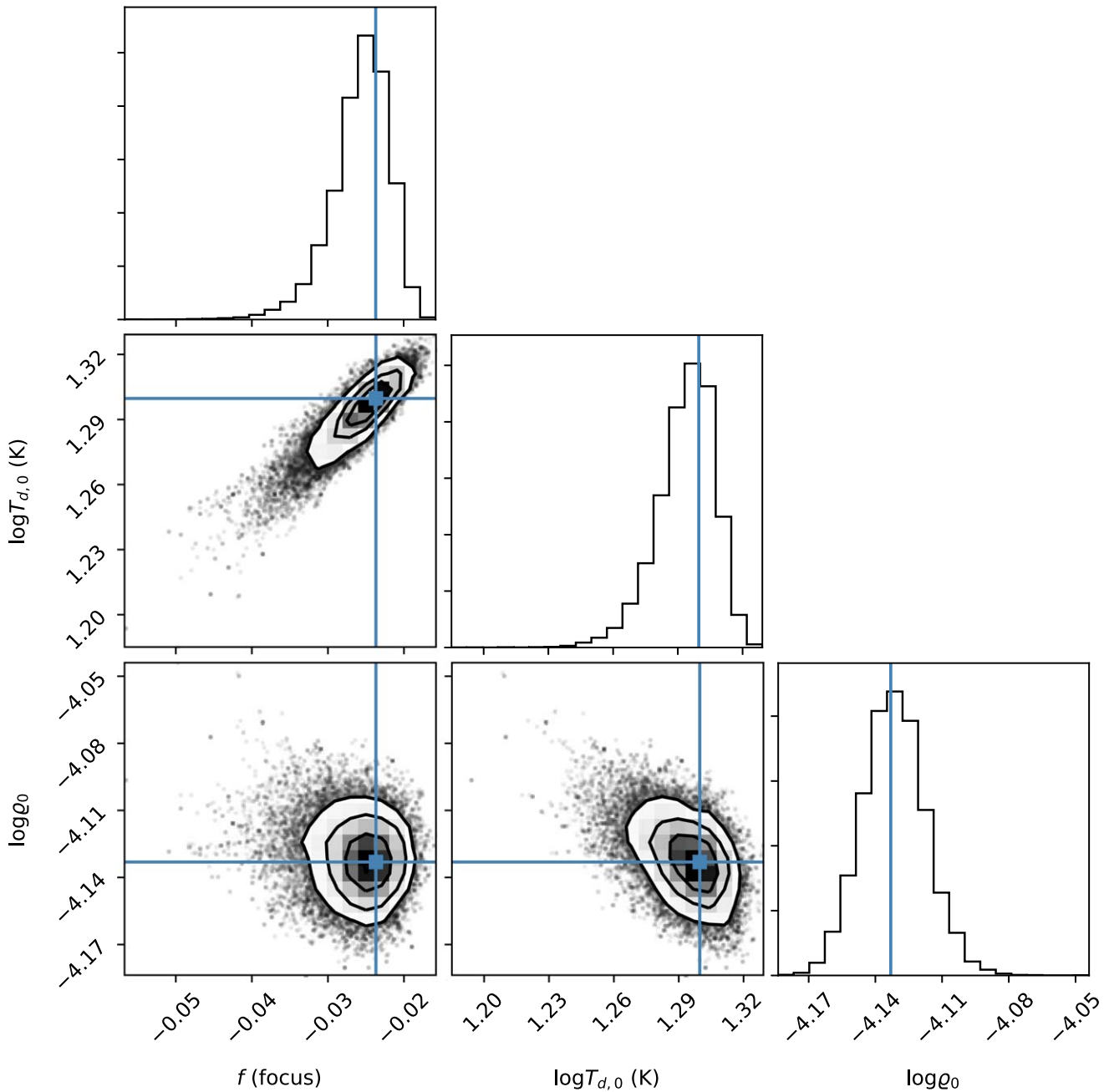
Figure 8. Corner plot of the posterior distributions of the variables in Equation (1). It is unclear whether the focus parameter f has any physical significance, and if so, what it might be.

of 20 K also looks at first glance like a sort of preferred temperature, but as most of this concentration is occurring in just three regions, we are skeptical of the significance. Next, we refer readers to Figure 10 in Muñoz Caro et al. (2010) and Figure 9 in Cazaux et al. (2017) to visualize how the gas-phase CO concentration varies with substrate temperature (the temperature-programmed desorption diagrams). These figures show that the distribution has a sharp peak in CO concentration between 27 and 30 K atop a much broader, lower distribution—except where the figure from Cazaux et al. (2017) shows that the sharper desorption peak can nearly disappear into the broader distribution if the CO ice is deposited at relatively high ($\sim$27 K) temperatures. On the other hand, the figure from Muñoz Caro et al. (2010) shows that a lower substrate temperature upon CO ice deposition allows thermal CO

desorption to start at lower temperatures, with escaping H_2 further encouraging CO desorption to begin around 15 K rather than somewhere between 20 and 25 K. If the physical quantities in Figure 7 are in fact comparable to the quantities plotted in these two publications, the shape of the $[N_{CO}/N_{H_2}]$–T_d curve is a surprisingly good qualitative reflection of how one might expect natural CO ice to be deposited, and later sublimate, given the temperature–density anticorrelation discussed in Section 3.1. The quick rise with flat or downward concavity in CO abundance between 15 and 20 K suggests that the surface layers of CO ice in depleted clumps are weakly bound and infused with trapped H_2. The rest of the temperature–abundance distribution lacks the sharp peak near 30 K indicative of CO ice deposited either at fixed temperatures much below 27 K or at decreasing temperatures from inside out as in Cazaux et al. (2017), Figure 8.
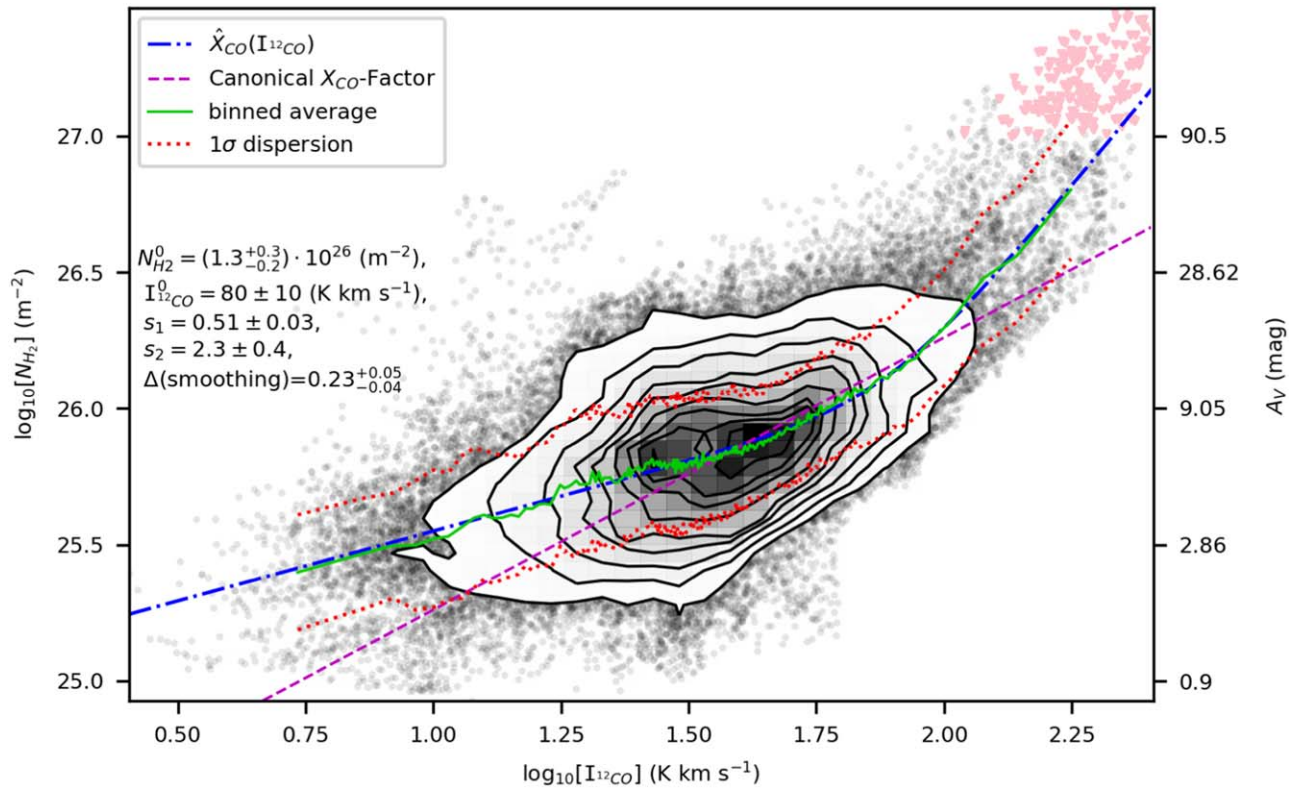
Figure 9. Log–log 2D histogram of N_{H_2} as a function of $I_{^{12}CO}$, the ratio of which is the X_{CO} factor. Overlaid are the binned average (solid green line), the 1σ dispersion (dotted red lines), the classical X_{CO} factor (dashed magenta line), and the fit to Equation (2) (dashed–dotted blue line). To distinguish our fitted model from the classical constant X_{CO}, we denote the model $\hat{X}_{CO}(I_{^{12}CO})$. Pink downward-pointing triangles are points from a saturated patch of Region 13 where column densities are likely to be upper limits.

However, this peak seems unlikely to be observed in nature regardless of T_d at the point of CO ice deposition—it appears to be an artifact of the lack of UV photons or cosmic rays that would stochastically push some of the CO molecules over the desorption activation barrier before the substrate (dust) temperature rises to meet the activation barrier, releasing all but the deepest monolayer(s) of CO in quick succession. All of this suggests that the gas-phase CO abundance should fall toward the center of a prestellar clump and rise again as embedded protostars form.

Despite the apparent goodness of fit in Figure 7, the parameter $\log_{10} \varrho_0$ puts a floor under N_{H_2} derived from CO. Equation (1) is well suited for data in the regime where CO is depleted owing to freeze-out, but it is not recommended for use in tandem with the power-law $I_{^{12}CO}-N_{H_2}$ relationship in Barnes et al. (2018) in gas with $N_{H_2} \lesssim 3 \times 10^{25}$ m^{-2}. Its greatest utility will likely be in giving observers in the submillimeter to millimeter range a new method to estimate dust temperatures when observations sampling the peak of the SED are not available.

3.3. Rethinking the X_{CO} Factor

Laboratory studies and simulations of how strongly the CO abundance varies as a function of temperature and radiation field strength suggest that it should vary by upward of three orders of magnitude (see Section 1). Moreover, regional red- and blueshifts of the ^{12}CO line relative to the ^{13}CO, C^{18}O, and HCO$^+$ lines observed in Paper III and Paper IV suggest that the ^{12}CO line is so universally opaque that it merely traces the surface of last scattering, rather than encoding the optical depth

through the whole cloud in the line wings. That means that physical conditions derived from ^{12}CO observations may not be consistent with ^{13}CO or C^{18}O or applicable to the cloud interior. At least insofar as H$_2$ column density is concerned, optically thin thermal dust emission offers the chance to directly calculate an X_{CO} factor expression that compensates for the tendency of low-excitation ^{12}CO lines to saturate or become optically thick.

3.3.1. Analysis

After computing pixel-by-pixel maps of N_{H_2} from dust SED fitting (hereafter denoted $N_{H_2}^{dust}$ to distinguish it from N_{H_2} calculated using CO) as per PBV2019, we simply aggregated all the data with naive uncertainties of 15% or less and plotted them against $I_{^{12}CO}$ as shown in Figure 9. The pink triangles are points from BYF 128b and 126a, where saturation at 250 μm made the SEDs poorly sampled. Ordinarily the slope of the three SPIRE data points drives the fitted SED to slightly overshoot the 160 μm data and slightly undershoot the 70 μm data owing to nonthermal contaminant emission in the latter filter; without the 250 μm point, the fitting routine tends to downweight the 70 μm data further and make the SED drop more steeply at 160 μm, nudging the amplitude of the curve higher while lowering the fitted temperature. The net effect is an increase in the reported N_{H_2}; hence, the data marked by pink downward-pointing triangles are upper limits.

To this distribution we fit a broken power law (dashed–dotted blue line in Figure 9, labeled $\hat{X}_{CO}(I_{^{12}CO}^0)$) with a smoothed transition of the form
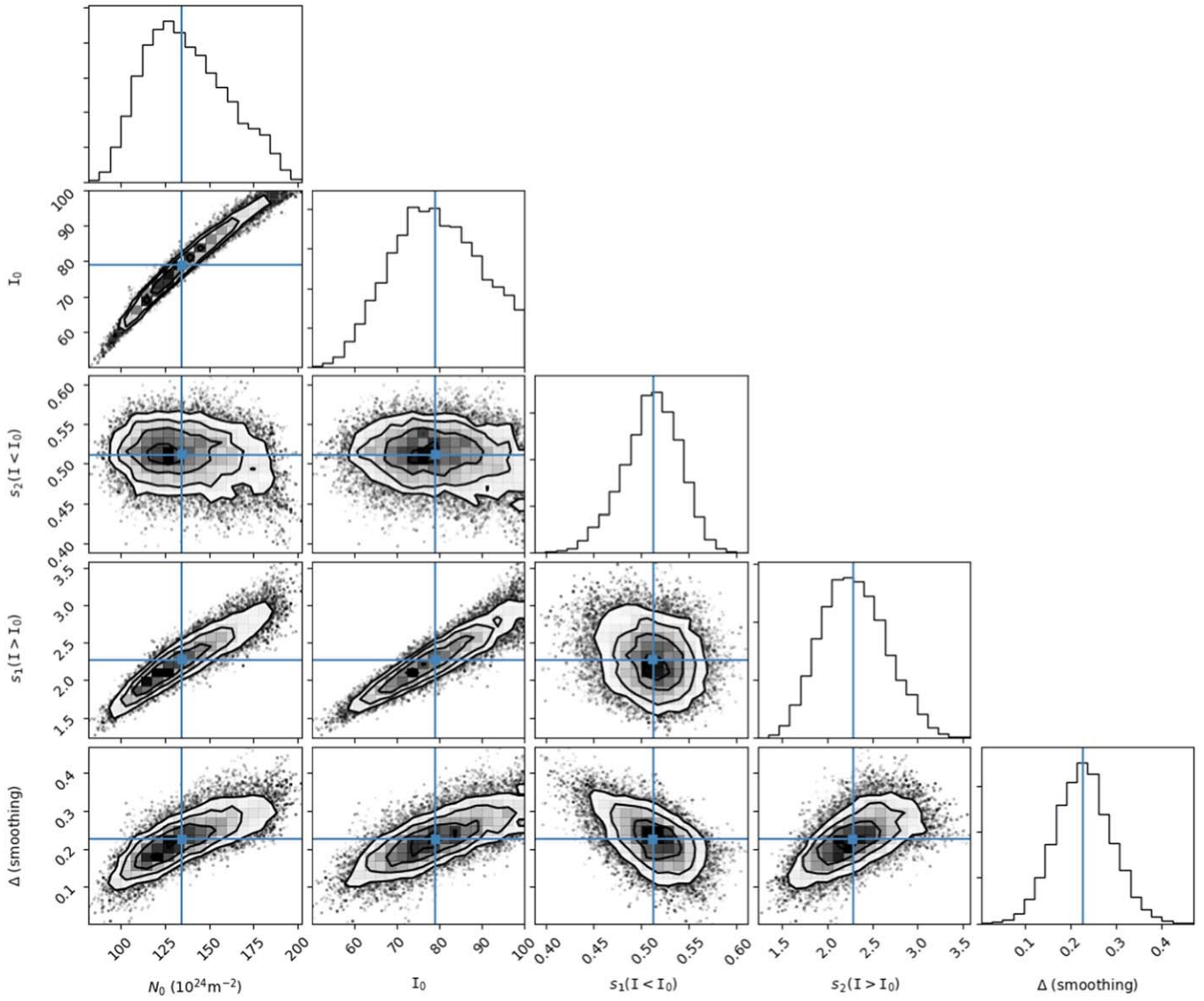
Figure 10. Posterior distributions of the free parameters of Equations (2) and (3).

$$N_{H_2} = N_{H_2}^0 I_\star^{s_1} \left[\frac{1}{2} + \frac{I_\star^{1/\Delta}}{2} \right]^{\Delta(s_2 - s_1)}, \qquad (2)$$

where

$$I_\star = \frac{I_{^{12}CO}}{I_{^{12}CO}^0} \qquad (3)$$

is the integrated CO line intensity divided by the transition point (indicated by the superscript zeros) between power laws in $I_{^{12}CO}$, $N_{H_2}^0$ is the H_2 column density at $I_{^{12}CO}^0$, and s_1 and s_2 are the power-law exponents to the left and the right of the transition point, respectively. Δ is a smoothing parameter defined such that if x and y denote the abscissa and ordinate, respectively, then $\Delta \approx 0.5 \log_{10}(x_2 - x_1)$, where $y(x \lesssim x_1) \propto x^{s_1}$ and $y(x \gtrsim x_1) \propto x^{s_2}$. In other words, Δ describes the half-width of the data range, in log-space, inside of which neither power-law component dominates enough to ignore the other. The equations and definitions above are essentially the same as the Astropy modeling module used to fit them, `SmoothlyBrokenPowerLaw1D` (Astropy Collaboration et al. 2013, 2018),

but in all of our equations and figures, we change the signs of the power-law exponents to be more intuitive. Visually, the goodness of fit can be judged by comparing the fit (again, the dashed–dotted blue line) with the binned average (solid green line). The binned average and the 1σ dispersion around it (dotted red lines) were computed such that each bin has $\lceil 2n^{2/5} \rceil$ data points (assumed equiprobable), where n is the total number of points, and the bins are positioned so that the leftover data points are roughly equally distributed between each end of the distribution. Equation (2) is technically not an expression of X_{CO}—to get an expression for X_{CO} in the usual units, the entire equation must be divided by $I_{^{12}CO}$. For comparison of the power-law exponents to those of other studies, it is enough to simply subtract 1 from s_1 and s_2. We fit the expression as above because when we tried to fit $N_{H_2}/I_{^{12}CO}$ directly, s_2 was consistently much too small.

As with the $[N_{CO}/N_{H_2}]$–T_d relation, we minimized the negative log-likelihood function over the parameters of Equation (2), assuming Gaussian uncertainties and flat priors, and produced the posterior distributions shown in Figure 10
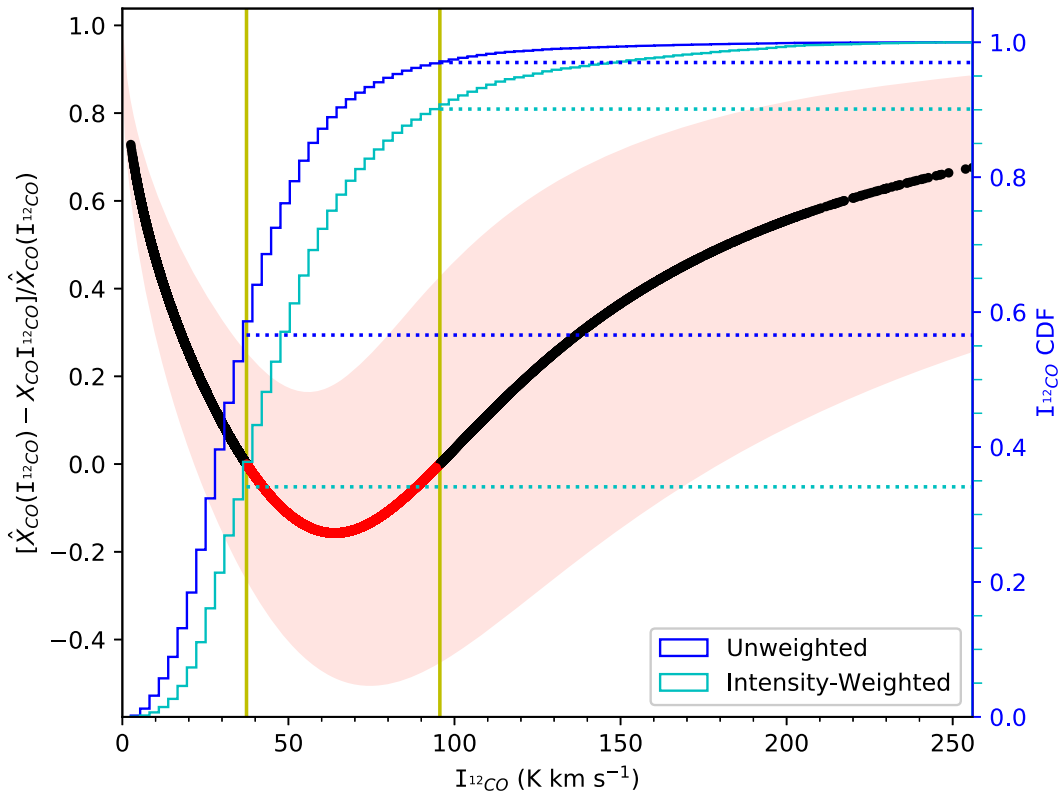
Figure 11. Fractional difference in derived N_{H_2} using the constant X_{CO} factor and our smoothed broken power law, $\hat{X}_{CO}(I_{12_{CO}})$. The blue and cyan stepped histograms are the unweighted and $I_{12_{CO}}$-weighted cumulative distribution functions of $I_{12_{CO}}$ to give an idea of what fraction of N_{H_2} calculations will be over- or underestimated by using the constant X_{CO} factor, and at what ranges of of $I_{12_{CO}}$. The pink filled range spans the 1σ variation in all of the fitted parameters of $\hat{X}_{CO}$. The vertical gold lines bracket the range of $I_{12_{CO}}$ where the constant X_{CO} factor overstates N_{H_2}, and the dotted blue and cyan lines help show what fraction of pixels fall in that range.

using emcee. We find that $N_{H2}^0 = (1.3^{+0.3}_{-0.2}) \times 10^{26}$ (m^{-2}), $I_{12_{CO}}^0 = 80 \pm 10$ (K km s^{-1}), $s_1 = 0.51 \pm 0.03$, $s_2 = 2.3 \pm 0.4$, and $\Delta = 0.23^{+0.05}_{-0.04}$. We used inverse-$\sigma$ weighting in the minimization routine, as opposed to the more typical inverse-variance weighting used in the fit of the $[N_{CO}/N_{H_2}]$–T_d relationship, because the points far from the mean can still be highly significant. It is also worth noting that the range of variation in intrinsic clump size is larger than the range of distances, so resolution is not expected to play a major role in the shape of the distribution overall.

Figures 9 and 11 make it abundantly clear that the relationship between $I_{12_{CO}}$ and N_{H_2} is not linear, though there is a fairly wide range of intermediate $I_{12_{CO}}$ values where N_{H_2} calculated with a constant X_{CO} factor are well within the 1σ dispersion. Note the exquisite agreement of the fit of Equation (2) with the binned average along the latter's entire length in Figure 9. To better show what is being missed by computing N_{H_2} using a constant X_{CO} factor, Figure 11 shows the difference between that and N_{H_2} derived using Equation (2), normalized by the latter and plotted as a thick black and red curve. The pink filled area represents the combined uncertainty in the difference given the uncertainties of the five free parameters of Equation (2). At the highest and lowest values of $I_{12_{CO}}$, the traditional X_{CO} factor may miss upward of 60% of the total mass in H_2, whereas for intermediate values of $I_{12_{CO}}$ the constant X_{CO} factor may actually overestimate the mass by up to 20%. On the same plot we have also included intensity-weighted (cyan) and equiprobable (blue) cumulative histograms of $I_{12_{CO}}$ on the secondary axis for all good pixels in the CHaMP sample and have drawn dotted lines to benchmark the percentiles

(for lack of a better word) against the difference curve on the primary axis so readers can see for what fractions of the data the traditional X_{CO} factor overstates and understates N_{H_2}.

Sixty percent of all pixels in the CHaMP sample have N_{H_2} greater than predicted by the standard X_{CO} factor. Of these 60% of pixels, more than 90% are in the $s_1 = 0.51 \pm 0.03$ regime, where the difference between using a constant X_{CO} factor and using Equation (2) is most statistically significant. The remaining $\lesssim 10\%$ of pixels with N_{H_2} greater than predicted by the standard X_{CO} factor are in the high-$I_{12_{CO}}$ $s_2 = 2.3 \pm 0.4$ regime of the broken power law. In the s_2 regime, where large increases in N_{H_2} produce only small changes in $I_{12_{CO}}$, optical depth increases proportionally with excitation temperature (T_{ex}), which approaches T_d at these column densities. The $s_1 = 0.51 \pm 0.03$ regime can only be a consequence of how radiative transfer works in moderately dense gas where CO is present but in a very low excitation state. Where CO is sufficiently subthermal, its optical depth will rise as the excitation temperature falls, at least until the gas is too diffuse to effectively shield the CO from destruction (see also, e.g., Peñaloza et al. 2017). If CO dissociation was the main cause of deviation from the standard X_{CO} factor, one would expect that $I_{12_{CO}}$ would drop off with falling column density superlinearly instead of sublinearly (indeed, as we discuss in Section 3.3.2, this is a predicted third regime that occurs below the column densities we chose to consider). To be fair, observations of low-excitation, low-opacity CO will always be subject to sensitivity limits, which bias observations of low-excitation CO toward areas where the CO is still optically thick. However, per Paper IV, CO observations should be complete down to

$10 \, \mathrm{K \, km \, s^{-1}}$, and we were aggressive in our continuum background subtraction to limit inclusion of incompletely sampled diffuse gas.

That the form of the $I_{^{12}CO} - N_{H_2}$ relationship has (at least) two power-law regimes with a transition region meshes well with what Barnes et al. (2018) found and the similar analysis of ThrUMMS data by P. J. Barnes et al. (2021, in preparation) with respect to the $I_{^{12}CO} - N_{CO}$ relationship. The range of physical conditions in which ^{12}CO is optically thin is narrow: the only CHaMP data with $\tau_{^{12}CO} \lesssim 1$ had $1 \, \mathrm{m^{-2}} \lesssim N_{CO} \lesssim 2 \times 10^{20} \, \mathrm{m^{-2}}$, and the minimum reliable $\tau_{^{12}CO}$ is about 4 (Barnes et al. 2018). Much less than 10% of the CHaMP sample has N_{CO} in that range; ^{13}CO and sometimes C^{18}O were needed to recover N_{CO} in the overwhelming majority of pixels. Most of the data follow two trends in N_{CO} versus $I_{^{12}CO}$ depending on the ^{12}CO excitation temperature, denoted T_{ex}. In the strongly subthermal regime (typically with $T_{ex} < 10 \, \mathrm{K}$), as T_{ex} falls toward the ^{12}CO brightness temperature minus the temperature of the cosmic microwave background, the optical depth spikes and N_{CO} becomes nearly independent of $I_{^{12}CO}$ (equivalently, $N_{H_2} \propto X_{CO}^s$, where s goes to -1 for low T_{ex}). For excitation temperatures well in excess of about $10 \, \mathrm{K}$, N_{CO} approaches an $I_{^{12}CO}^2$ dependence. The similarity of both power-law exponents in Equation (2) to those of the velocity-resolved N_{CO} versus $I_{^{12}CO}$ plots in Barnes et al. (2018), within their mutual margins of uncertainty, seems unlikely to be a coincidence and will be explored in future work by this collaboration.

Our findings are of imminent import to the question of how much molecular gas in a cloud is CO-dark, only accountable via other tracers like dust. CO-dark gas is thought to be relatively diffuse gas in the envelopes of MCs where gas densities are high enough for H$_2$ to self-shield, but not high enough for CO to be shielded (Blitz et al. 1990; Wolfire et al. 2010). As mentioned in the introduction, estimates of the CO-dark gas fraction vary wildly from 20% to upward of 70% (Pineda et al. 2013; Langer et al. 2014). Unfortunately, to truly put this consideration to the test, observers must be able to resolve the width of a CO-dark envelope, not just the width of an MC. This has been done in Taurus (Xu et al. 2016). However, without the benefit of an accurate and appropriately varying CO abundance, the equation for the dark gas fraction is dubious.

The implications of this and similar studies go far beyond the obvious effects on measurements of CO-dark gas and star formation efficiency. The density of a parcel of molecular gas is the chief determinant of any physical or chemical evolutionary timescale. Take, for example, the rate at which either an individual MC or an entire galactic disk is converted into stars—intuitively, the rate of H$_2$ consumption is determined by how fast the gas collapses, which, for an extended mass like a cloud, must be dictated by the gas density. The Kennicutt–Schmidt (KS) law (Schmidt 1959, 1963; Kennicutt 1998) quantifies these expectations—the eponymous studies and their successors show that the star formation rate per unit area is proportional to a slightly superlinear power law in H$_2$ column density. These studies rarely include other isotopologues of CO. If the X_{CO} factor is actually a broken power law, that could change the exponent of the KS law or even its entire functional form. It would be interesting to see if the recent case made in Kennicutt & De Los Reyes (2021) for a bimodal or broken KS law could be tied to the broken power-law X factor

in the sense that the high-density, high-$I_{^{12}CO}$ gas is analogous to the bulk of the CO-bright gas in starburst galaxies. However, that is beyond the scope of this paper.

3.3.2. Comparison with Literature

Shetty et al. (2011a) and Shetty et al. (2011b) collectively describe perhaps the most thorough investigation of the X_{CO} factor in synthetic Galactic MCs, incorporating MHD simulations with non-LTE radiative transfer and the non-LTE chemical modeling described in Glover et al. (2010) and Glover & Mac Low (2011). This series focuses on a range of densities that top out in the middle of the range that CHaMP probes, about $10^{26} \, \mathrm{m^{-2}}$, and extend down to column densities about two orders of magnitude lower than any of the CHaMP data that we trust. Where the CHaMP data overlap in N_{H_2} (or A_V) with the models in Shetty et al. (2011b), the model initialized with an H$_2$ volume density $n \geqslant 3 \times 10^6 \, \mathrm{m^{-3}}$ had roughly the same slope in the log for $N_{H_2} \gtrsim 10^{26} \, \mathrm{m^{-2}}$ as the running mean in the left panel of Figure 12: 1.2 to our 1.3. The normalization $N_{H2}^0/I_{^{12}CO}^0$ (the minimum in $\hat{X}_{CO}(I_{^{12}CO})$ and also the power-law transition point) from our model is within about 0.1 dex of the inflection point of their minimum in X_{CO} as well. In the right panel of Figure 12, where we color-code the data by $I_{^{12}CO}$ and overlay the model $\hat{X}_{CO}(I_{^{12}CO})$, it becomes apparent that the data distribution is hiding the turnover to the regime where the slope of $\hat{X}_{CO}(I_{^{12}CO})$ trends negative. Plotting the X_{CO} factor as a function of N_{H_2} is natural for theoretical calculations, but it obscures a very real concern for observational astronomers that the right panel of Figure 12 is meant to demonstrate. That is, for most of the range of H$_2$ column densities one would want to probe, there is nearly a factor of 30 difference between the largest and smallest values of N_{H_2} that could be derived from a given value of $I_{^{12}CO}$.

The agreement of our results with Shetty et al. (2011a) and Shetty et al. (2011b), at least with the solar-metallicity model initialized $n \geqslant 3 \times 10^6 \, \mathrm{m^{-3}}$, is remarkable for several reasons, not least of which is that Equation (2) incorporates no other physics than the two LTE radiative transfer analyses required to do (1) the SED fitting and (2) the multi-CO line fitting. Their models fix the ISRF at 1.7 Habing units, far less than what is expected to be impinging on the CHaMP clumps around the Carina Nebula, NGC 3576, NGC 3603, and a number of other H II regions in our sample. Their analysis of X_{CO} as a function of CO abundance in Shetty et al. (2011a) allows for photodissociation, but apparently not depletion; however, only one model occupies the parameter space above $N_{H_2} \gtrsim 3 \times 10^{26} \, \mathrm{m^{-2}}$, and they only explore the $X_{CO} - [N_{CO}/N_{H_2}]$ relationship for $N_{H_2} \leqslant 3 \times 10^{26} \, \mathrm{m^{-2}}$. Still, it is worth noting that whether $[N_{CO}/N_{H_2}]$ was allowed to vary, fixed at 10^{-4}, or fixed at 10^{-5}, the normalization may have changed, but the slope of $\log X_{CO}$ versus $\log N_{H_2}$ stayed roughly the same for $N_{H_2} \gtrsim 3 \times 10^{25} \, \mathrm{m^{-2}}$ ($A_V \sim 3^m$). That suggests that the change of power-law exponent is an effect of shielding, and that while the normalization may change, the s_2 regime of Equation (2) is robust to more than an order of magnitude of variation in CO abundance. For the Milky Way−type galaxies at least, then, it should be generally safe to assume that N_{H_2} is approximately proportional to the square of $I_{^{12}CO}$ where ^{12}CO is bright (a few $\times \, 10 \, \mathrm{K \, km \, s^{-1}}$), and other CO isotopologues are not available. The slope of the s_1 regime, by contrast, appears highly sensitive to the CO abundance, whose characterization is aided by dust temperature, but is ultimately incomplete
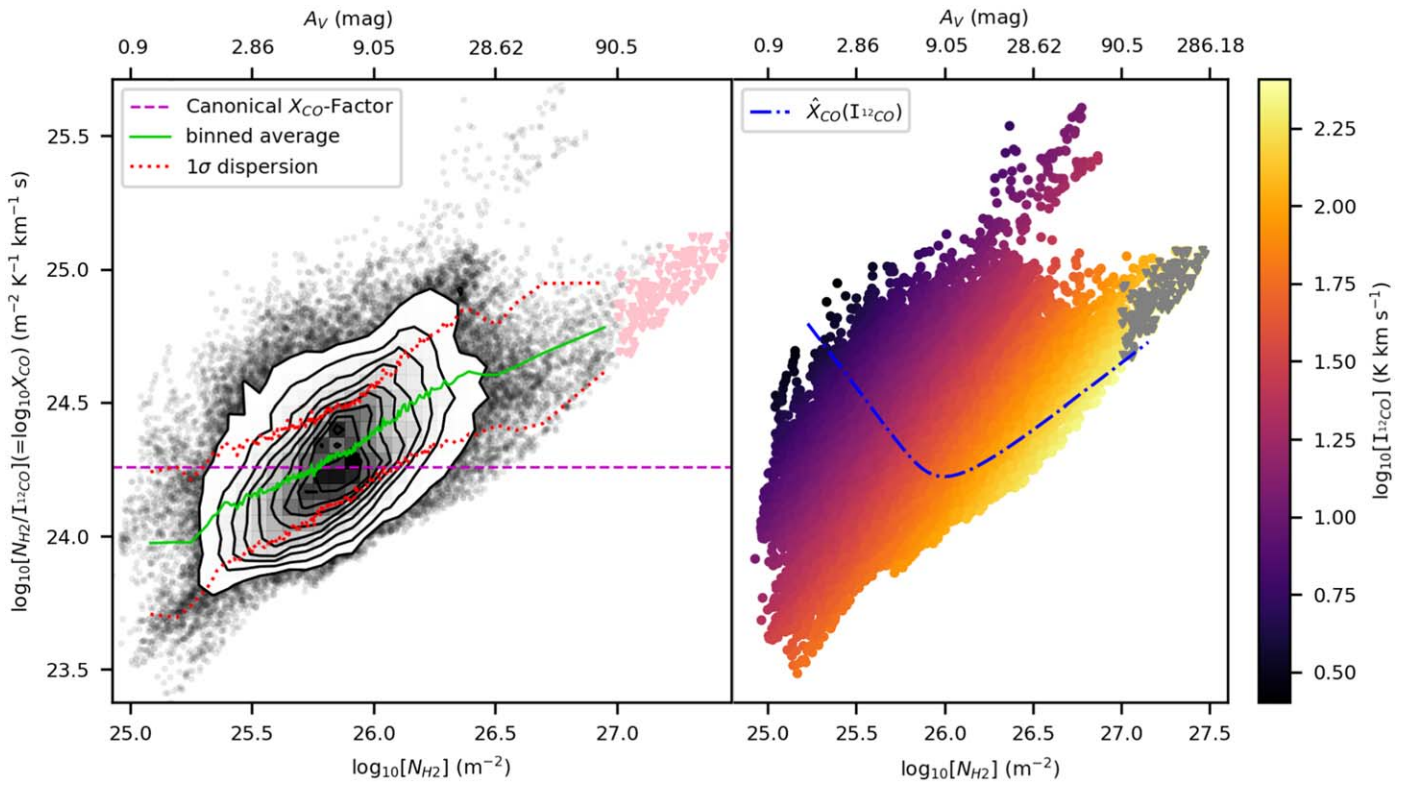
Figure 12. Plots of the X_{CO} factor as a function of N_{H_2} for comparison to synthetic models, one color-coded by $I_{^{12}CO}$. The left panel shows a 2D histogram of the CHaMP data overlaid with the binned average (solid green line), 1σ dispersion (dotted red lines), and classical X_{CO} factor (dashed magenta line), so the slope can be measured by eye. The right panel shows the CHaMP data again as a scatter plot color-coded by $I_{^{12}CO}$, with the $\hat{X}_{CO}$ curve overlaid as a dashed–dotted blue line, to show how orientating and normalizing the data this way obscures the $I_{^{12}CO}$ dependence of X_{CO}. The blue $\hat{X}_{CO}$ curve was generated by dividing the ordinate (N_{H_2}) in Figure 9 by the abscissa ($I_{^{12}CO}$) and plotting the quotient ($\hat{X}_{CO}$) as a function of the ordinate.

without understanding the ISRF dependence. The effects of sensitivity limits are also under investigation (Vázquez-Semadeni et al., private communication), but our sampling should be complete for $I_{^{12}CO} \gtrsim 10$ K km s^{-1}.

The Shetty et al. studies did not cover the effects of varying the ISRF on the X_{CO} factor or the effects of CO line velocity width. These issues were tackled in Feldmann et al. (2012), who used essentially the same underlying chemical models and simulation techniques to expand on the works by the Shetty et al. series above. Feldmann et al. (2012) found that at large N_{H_2} (A_V) the X_{CO} factor becomes directly proportional to N_{H_2} if the CO line width is constant, or proportional to the square root of N_{H_2} if the CO line width of the cloud is bound and in virial equilibrium. A look at the slope of the blue dotted–dashed $\hat{X}_{CO}(I_{^{12}CO})$ line in Figure 12 (right) suggests that a virial distribution of CO line velocity widths more accurately describes reality: over the range $10^m < A_V < 100^m$, $\hat{X}_{CO}(I_{^{12}CO})$ increases by about half a dex. However, the trends in the data and the scatter essentially rotate 90° in this plot just shy of $A_V \sim 10^m$ or $\log[N_{H_2}] \sim 26$ m^{-2}. The scatter around the low-N_{H_2} side of the function spans almost the entire range of N_{H_2} and is parallel to the trend on the high N_{H_2} side—the rise in the X_{CO} factor toward low column densities would have gone unseen had we not modeled X_{CO} as a function of $I_{^{12}CO}$ instead of N_{H_2}. Not only is the anticorrelation between the X_{CO} factor and N_{H_2} at low column densities real, but the enormous scatter also appears to be reproduced in the Feldmann et al. (2012) study with a variety of ISRF strengths ranging from 0.1 to 100 G_0 in Habing (1968) units. However, after they divided out the metallicity and ISRF dependencies, we observed some

statistically significant differences between their plot of X_{CO} versus $I_{^{12}CO}$ (Feldmann et al. 2012, Figure 4, bottom right) and ours (Figure 9, subtracting one from both exponents). Their power-law transition point is closer to 30 K km s^{-1}, compared to our 80 ± 10 K km s^{-1}, and while their high-$I_{^{12}CO}$ power-law exponent (s_2) is within 1σ of ours, their low-$I_{^{12}CO}$ power-law exponent (s_1) is almost twice as steeply negative as ours. It seems highly likely that these differences are explainable by the fact that we did not have ISRF information to divide out: averaging over several steep trends with varying vertical-axis intercepts will tend to flatten the slope. Moreover, as the Feldmann et al. (2012) study makes clear, stronger ambient UV irradiation pushes the power-law break point to higher N_{H_2} and larger $I_{^{12}CO}$. Therefore, while the differences between our model and theirs are statistically significant, the findings of our studies seem physically consistent.

Previous observational studies of X_{CO} factor variance have mostly relied on dust extinction and heavily favored nearby, lower-mass star-forming regions, like the Pipe Nebula (Lombardi et al. 2006), Perseus MC (Pineda et al. 2008; Lee et al. 2014; Tafalla et al. 2021), the Taurus MC (Pineda et al. 2010), and the California MC (Kong et al. 2015). Even including similar analysis of the Orion MC complex by Ripple et al. (2013), none of these studies probe N_{H_2} values even half as high as the CHaMP sample. Still, only data for highly irradiated portions of Orion and the California MC fail to show the $I_{^{12}CO}$–N_{H_2} relationship entering the equivalent of our fit's s_2 regime, i.e., $I_{^{12}CO}$ becoming less sensitive to increasing A_V starting between 1^m and 10^m. Moreover, Lee et al. (2014) and Ripple et al. (2013) also find that, as with our s_1 regime, the

trend at low N_{H_2} (A_V of 1 to a few magnitudes) is for $I_{^{12}CO}$ to be more sensitive to changes in N_{H_2} than the canonical X_{CO} factor would suggest, whereas Lombardi et al. (2006) find the opposite to be true in the Pipe Nebula for $A_V \lesssim 1$ and $I_{^{12}CO} < 40$ K km s^{-1}. In the Perseus cloud, both Pineda et al. (2008) and Lee et al. (2014) find that all parts of the cloud enter the s_2 regime at $A_V \gtrsim 4^m$ starting at $20K$ km s$^{-1} < I_{^{12}CO} < 60$ K km s^{-1}. However, unlike Lee et al. (2014), ^{12}CO line emission data from Pineda et al. (2008) appear to follow the classical X_{CO} factor exactly, suggesting optically thin emission. This seems to be due to their use of curve-of-growth analysis on ^{12}CO to derive N_{CO} and variations in the ratios of ^{13}CO and ^{18}CO to ^{12}CO, rather than performing simultaneous radiative transfer on the three isotopologues assuming constant isotope ratios. In Kong et al. (2015), 11 out of 17 equal-sized segments of the California cloud have roughly the same measured $I_{^{12}CO}$ over the entire range of A_V ($<5^m$–35^m), with $I_{^{12}CO}$ hovering between 10 and 20 K km s^{-1}; two more segments closer to the active star-forming part become optically thick in ^{12}CO emission at A_V between 5^m and 10^m (N_{H_2} of $(6-10) \times 10^{26}$ m^{-2}) and $I_{^{12}CO}$ just shy of 40 K km s^{-1}; and the remaining four segments abutting the embedded cluster fan out in A_V–$I_{^{12}CO}$ space such that the standard X_{CO} factor might actually overestimate N_{H_2} in a majority of pixels. Most notably, Kong et al. (2015) find a slope $s_2 \sim 2.4$ among the quiescent parts of the California MC, well within the margin of uncertainty for our value of s_2.

Most of the qualitative discrepancies between our data distribution in $I_{^{12}CO}$–N_{H_2}-space and data from the aforementioned observational studies lie in the width and position of the transition zone and the behavior of the data at low values of $I_{^{12}CO}$ and N_{H_2} (extinction). Virtually all the aforementioned studies find narrower transition zones than ours, which is to be expected since our data set is aggregated over a larger area than the previous studies. Most of the other studies' data also enter the high-$I_{^{12}CO}$, high-N_{H_2} regime at lower N_{H_2} than our data for high-mass prestellar clumps, also as expected given that high-mass star formation tends to occur in clouds that are both denser and more strongly irradiated. Aside from Kong et al. (2015) and Tafalla et al. (2021), the latter of whom fit each CO isotopologue separately, most of the studies lacked the statistics to fit slopes to their s_2 regimes, even if the data clearly suggested a turnover.

Other attempts have been made by Okamoto et al. (2017) and Kalberla et al. (2020) to combine H I data with CO and dust emission. Of these, the findings of Okamoto et al. (2017) from the Perseus cloud most closely approach our results: in the $I_{^{12}CO}$ regime that overlaps our data ($I_{^{12}CO} < 30$ K km s^{-1}), they also find that X_{CO} is higher at lower $I_{^{12}CO}$ values (recall that dividing N_{H_2} by $I_{^{12}CO}$ yields the same power-law form, except all the exponents are reduced by 1; thus, our derived exponent on the low-$I_{^{12}CO}$ side is -0.49). However, their data, taken as they were from a single giant MC at high resolution, show significant substructure in the $I_{^{12}CO}$–X_{CO} plane for $I_{^{12}CO} < 15$ K km s^{-1} and mostly plateau for $I_{^{12}CO} \gtrsim 15$ K km s^{-1}, where they indicate that the CO data are optically thick. The substructure at $I_{^{12}CO} < 15$ K km s^{-1} and relative sparseness of data at $I_{^{12}CO} \gtrsim 15$ K km s^{-1} make it difficult to determine whether the apparent change of slope is significant. If one shifted our power-law X_{CO} fit along the dashed magenta line representing the constant X_{CO} factor in Figure 9 until the slope transition starts around 15 K km s^{-1}, the fit would still be

within the 1σ dispersion, so we do not consider our results to be inconsistent with those of Okamoto et al. (2017) at this time.

While Kalberla et al. (2020) mostly worked in a drastically different temperature regime, they bring up an alternative interpretation of the data that should be mentioned for the sake of completeness. They assumed constant ratios of CO to H$_2$ and A_V to H I and used CO, A_V, and H I to map the distribution of CO-dark gas and fit a temperature-dependent "correction factor" for the relationship between extinction and hydrogen column density. This correction factor is essentially a variable gas-to-dust ratio, which is the main alternative explanation for our CO abundance maps. To be fair, if CO is depleting onto grains, grain growth is occurring by definition, although increases in grain size do not necessarily imply a decrease in grain number density. However, we still believe that the increase in X_{CO} at the highest densities is predominantly due to CO depletion, not a falling gas-to-dust ratio, because of how well changes in CO abundance with temperature track with those observed in the lab. Moreover, the distance to the Carina Tangent is such that Herschel images should not resolve the scales of individual protostellar disks, where dust settling and coagulation would occur.

The effects of CO excitation were partly addressed in Paper III and Barnes et al. (2015) and will be addressed further in a forthcoming paper by E. Vasquez-Semadini and P. J. Barnes (2021, in preparation). However, in light of a recent paper by Sofue & Kohno (2020), it seems worthwhile to clarify what we think is happening in regions where both N_{H_2} and $I_{^{12}CO}$ are low, given the benefit of T_d information. Shading the data in Figure 9 by T_d yields the distribution shown in Figure 13 (note that data may be incomplete for $I_{^{12}CO} < 10$ K km s^{-1}). The binned average temperature and its 1σ dispersion are plotted as red solid and dotted lines, respectively, against the second vertical axis. Note that the lowest average dust temperatures occur at middling values of $I_{^{12}CO}$ and moderately high values of N_{H_2}, rising toward both higher and lower values of $I_{^{12}CO}$. This seems to be a result of averaging over prestellar clumps that cool toward their centers and protostellar clumps that are both warmer toward their centers and systematically denser overall than their prestellar counterparts. The fact that T_d rises toward lower values of $I_{^{12}CO}$ as well as higher values suggests that the low $I_{^{12}CO}$ values can be explained by one of two possibilities: either CO is beginning to dissociate as gas becomes warmer and less dense, or the dust and excitation temperatures are decoupling and the CO is becoming subthermal, which tends to raise the CO optical depth (see also the discussion in Section 3.1.2 of Gong et al. 2018). In either case, CO should underestimate H$_2$, contrary to the interpretations of Sofue & Kohno (2020), and that is indeed what the slope of the low-$I_{^{12}CO}$ s_1 regime indicates. A more direct comparison of the dust and CO excitation temperatures is, however, outside the scope of this paper.

4. Conclusions

SED-fitting parameter maps for the complete CHaMP sample show that H$_2$ column density maxima usually coincide with dust temperature minima, implying that density enhancement/collapse and cooling must be contemporaneous phases in the evolution of prestellar clumps. However, protostellar clumps and externally irradiated clumps overlap prestellar clumps in the N_{H_2}–T_d plane. Eighty-four percent of clumps have anticorrelated N_{H_2} and T_d, and a few percent of clumps with positively correlated N_{H_2} and T_d are observably being
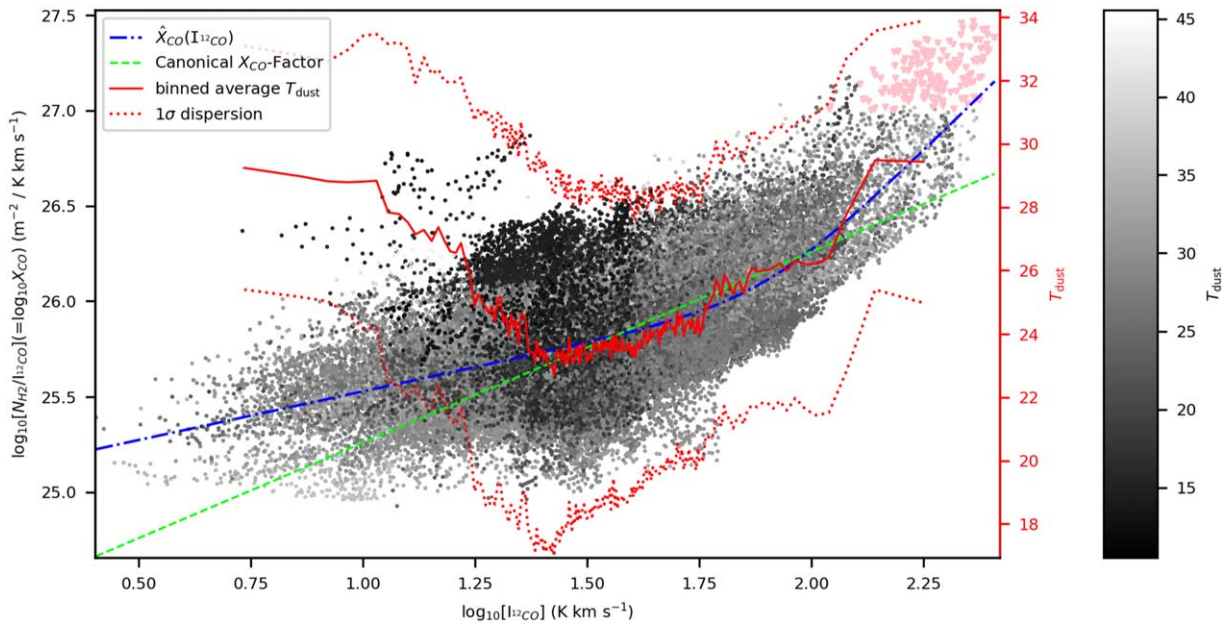
Figure 13. Similar to Figure 9, except all individual points are shown value-coded by T_d, and with the binned average T_d and its 1σ dispersion plotted as solid and dotted red lines, respectively. The dashed line showing the canonical X_{CO} factor is recolored in green for visibility. Sampling is complete down to $I_{^{12}CO} \sim$ 10 K km s^{-1}; data below that should be taken with caution.

heated and compressed by external radiation sources. Catalog matching is needed to determine whether these results are consistent with roughly 90% of prestellar clumps being genuinely quiescent, or only effectively so at the resolution of our observations.

We compared N_{CO} maps from Paper III, derived using multiple CO isotopologues, to N_{H_2} derived from dust emission and published here, and we mapped the computed CO abundance for the rest of the CHaMP sample not covered previously in PBV19. We find not only that there is no single CO-to-H_2 abundance ratio appropriate for all physical conditions possible in Galactic MCs but also that the CO abundance is a strong function of dust temperature, in line with laboratory experiments. The relationship has a dispersion of a factor of a few, and the dispersion seems to increase with temperature, as expected given that warmer pixels are dominated by gas in outer clump envelopes subject to varying degrees of external irradiation. Our empirical temperature–abundance relationship is parabolic in log-space, with a peak CO abundance of $7.4^{+0.2}_{-0.3} \times 10^{-5}$ per H_2 at $20.0^{+0.4}_{-1.0}$ K.

We show that the X_{CO} factor is significantly nonlinear: the standard constant X_{CO} factor yields H_2 column densities outside the 1σ dispersion of the CHaMP data for $I_{^{12}CO} < 10$ K km s^{-1} and $I_{^{12}CO} > 170$ K km s^{-1}, as well as for $A_V \lesssim 2$ and $A_V \gtrsim 28$. Our broken power-law fit to the X_{CO} factor has $N_{H_2} \propto I_{^{12}CO}^{0.51}$ for $I_{^{12}CO} \lesssim 70$ K km s^{-1}, $N_{H_2} \propto I_{^{12}CO}^{2.3}$ for $I_{^{12}CO} \gtrsim 90$ K km s^{-1}, and a smooth transition between. The larger of the two exponents is consistent with the simulations of Shetty et al. (2011b) and Feldmann et al. (2012), but the smaller exponent is somewhat smaller than expected for a fixed UV field strength. However, the simulations of Feldmann et al. (2012) show that the transition point is a function of local UV field strength, so averaging over many environments with a variety of UV field strengths is expected to broaden the transition region and reduce the exponent in the low-$I_{^{12}CO}$, regime. Compared to the constant X_{CO} factor, the broken power law ($\hat{X}_{CO}(I_{^{12}CO})$ for short) predicts N_{H_2} values

as much as 20% lower for $37 K$ km s$^{-1} < I_{^{12}CO} < 95$ K km s^{-1}, but higher by up to 60% for $I_{^{12}CO}$ outside of this range. More than half of all CHaMP data pixels are in the low-$I_{^{12}CO}$ regime where $N_{H_2} \propto I_{^{12}CO}^{0.51}$, and the increase in predicted N_{H_2} is most statistically significant.

ORCID iDs

Rebecca L. Pitts ⓘ https://orcid.org/0000-0002-7937-4931

References

Ababakr, K. M., Fairlamb, J. R., Oudmaijer, R. D., & van den Ancker, M. E. 2015, MNRAS, 452, 2566

Albacete Colombo, J. F., Méndez, M., & Morrell, N. I. 2003, MNRAS, 346, 704

Astropy Collaboration, Price-Whelan, A. M., Sipőcz, B. M., et al. 2018, AJ, 156, 123

Astropy Collaboration, Robitaille, T. P., Tollerud, E. J., et al. 2013, A&A, 558, A33

Bacmann, A., Lefloch, B., Ceccarelli, C., et al. 2002, A&A, 389, L6

Barbá, R. H., Roman-Lopes, A., Nilo Castellón, J. L., et al. 2015, A&A, 581, A120

Barnes, P. J., Hernandez, A. K., Muller, E., & Pitts, R. L. 2018, ApJ, 866, 19

Barnes, P. J., Hernandez, A. K., O'Dougherty, S. N., Schap, W. J., III, & Muller, E. 2016, ApJ, 831, 67

Barnes, P. J., Muller, E., Indermuehle, B., et al. 2015, ApJ, 812, 6

Barnes, P. J., Ryder, S. D., O'Dougherty, S. N., et al. 2013, MNRAS, 432, 2231

Barnes, P. J., Yonekura, Y., Fukui, Y., et al. 2011, ApJS, 196, 12

Batchelor, R. A., Caswell, J. L., Goss, W. M., et al. 1980, AuJPh, 33, 139

Beckwith, S. V. W., Sargent, A. I., Chini, R. S., & Guesten, R. 1990, AJ, 99, 924

Blitz, L., Bazell, D., & Desert, F. X. 1990, ApJL, 352, L13

Bolatto, A. D., Wolfire, M., & Leroy, A. K. 2013, ARAA, 51, 207

Borissova, J., Bonatto, C., Kurtev, R., et al. 2011, A&A, 532, A131

Brand, J., Blitz, L., & Wouterloot, J. G. A. 1986, A&AS, 65, 537

Braz, M. A., & Epchtein, N. 1983, A&AS, 54, 167

Braz, M. A., Gregorio Hetem, J. C., Scalise, E., Monteiro Do Vale, J., & Gaylard, M, J. L. 1989, A&AS, 77, 465

Bronfman, L., Nyman, L. A., & May, J. 1996, A&AS, 115, 81

Cappa, C., Niemela, V. S., Amorín, R., & Vasquez, J. 2008, A&A, 477, 173

Caselli, P., Walmsley, C. M., Tafalla, M., Dore, L., & Myers, P. C. 1999, ApJL, 523, L165

Caswell, J. L. 2004, MNRAS, 351, 279

Caswell, J. L., & Haynes, R. F. 1987, A&A, 171, 261

Cazaux, S., Martín-Doménech, R., Chen, Y. J., Muñoz Caro, G. M., & González Díaz, C. 2017, ApJ, 849, 80

Cutri, R. M., Skrutskie, M. F., van Dyk, S., et al. 2003, yCat, II/246

Cutri, R. M., Wright, E. L., Conrow, T., et al. 2012, Explanatory Supplement to the WISE All-Sky Data Release Products

Cutri, R. M., Wright, E. L., Conrow, T., et al. 2013, Explanatory Supplement to the AllWISE Data Release Products

Cyganowski, C. J., Whitney, B. A., Holden, E., et al. 2008, AJ, 136, 2391

Dame, T. M., Hartmann, D., & Thaddeus, P. 2001, ApJ, 547, 792

Dutra, C. M., & Bica, E. 2001, A&A, 376, 434

Dutra, C. M., Bica, E., Soares, J., & Barbuy, B. 2003, A&A, 400, 533

Egan, M. P., Price, S. D., Kraemer, K. E., et al. 2003, yCat, V/114

Feigelson, E. D., Getman, K. V., Townsley, L. K., et al. 2011, ApJS, 194, 9

Feldmann, R., Gnedin, N. Y., & Kravtsov, A. V. 2012, ApJ, 747, 124

Fontani, F., Giannetti, A., Beltrán, M. T., et al. 2012, MNRAS, 423, 2342

Foreman-Mackey, D., Hogg, D. W., Lang, D., & Goodman, J. 2013, PASP, 125, 306

Giveon, U., Sternberg, A., Lutz, D., Feuchtgruber, H., & Pauldrach, A. W. A. 2002, ApJ, 566, 880

Glover, S. C. O., Federrath, C., Mac Low, M.-M., & Klessen, R. S. 2010, MNRAS, 404, 2

Glover, S. C. O., & Mac Low, M.-M. 2011, MNRAS, 412, 337

Gong, M., Ostriker, E. C., & Kim, C.-G. 2018, ApJ, 858, 16

Grasdalen, G. L., Gehrz, R. D., Hackwell, J. A., Castelaz, M., & Gullixson, C. 1983, ApJS, 53, 413

Green, J. A., Caswell, J. L., Fuller, G. A., et al. 2012, MNRAS, 420, 3108

Gregorio-Hetem, J., Lepine, J. R. D., Quast, G. R., Torres, C. A. O., & de La Reza, R. 1992, AJ, 103, 549

Griffin, M. J., Abergel, A., Abreu, A., et al. 2010, A&A, 518, L3

Gum, C. S. 1955, MmRAS, 67, 155

Guzmán, A. E., Sanhueza, P., Contreras, Y., et al. 2015, ApJ, 815, 130

Habing, H. J. 1968, Bull. Astron. Inst. Netherlands, 19, 421

Harju, J., Lehtinen, K., Booth, R. S., & Zinchenko, I. 1998, A&AS, 132, 211

Hasenberger, B., Lombardi, M., Alves, J., et al. 2018, A&A, 620, A24

Hayashi, K., Mizuno, T., Fukui, Y., et al. 2019, ApJ, 884, 130

Helou, G., & Walker, D. W. 1988, Infrared Astronomical Satellite (IRAS) Catalogs and Atlases: The Small Scale Structure Catalog., Vol. 7

Hernandez, A. K., Tan, J. C., Caselli, P., et al. 2011, ApJ, 738, 11

Hildebrand, R. H. 1983, QJRAS, 24, 267

Hoffleit, D. 1953, AnHar, 0119, 37

Ishihara, D., Onaka, T., Kataza, H., et al. 2010, A&A, 514, A1

Juvela, M., Padoan, P., & Nordlund, Å. 2001, ApJ, 563, 853

Kahn, F. D. 1974, A&A, 37, 149

Kalberla, P. M. W., Kerp, J., & Haud, U. 2020, A&A, 639, A26

Kennicutt, R. C., J., & De Los Reyes, M. A. C. 2021, ApJ, 908, 61

Kennicutt, R. C., Jr. 1998, ApJ, 498, 541

Kong, S., Lada, C. J., Lada, E. A., et al. 2015, ApJ, 805, 58

Kramer, C., Alves, J., Lada, C. J., et al. 1999, A&A, 342, 257

Kuiper, R., Klahr, H., Beuther, H., & Henning, T. 2011, BSRSL, 80, 211

Lada, C. J., & Lada, E. A. 2003, ARAA, 41, 57

Langer, W. D., Velusamy, T., Pineda, J. L., Willacy, K., & Goldsmith, P. F. 2014, A&A, 561, A122

Lee, M.-Y., Stanimirović, S., Wolfire, M. G., et al. 2014, ApJ, 784, 80

Lombardi, M., Alves, J., & Lada, C. J. 2006, A&A, 454, 781

Ma, B., Tan, J. C., & Barnes, P. J. 2013, ApJ, 779, 79

Maercker, M., Burton, M. G., & Wright, C. M. 2006, A&A, 450, 253

Markwardt, C. B. 2009, in ASP Conf. Ser. 411, Astronomical Data Analysis Software and Systems XVIII, ed. D. A. Bohlender et al. (San Francisco, CA: ASP), 251

Molinari, S., Swinyard, B., Bally, J., et al. 2010a, A&A, 518, L100

Molinari, S., Swinyard, B., Bally, J., et al. 2010b, PASP, 122, 314

Mottram, J. C., Hoare, M. G., Lumsden, S. L., et al. 2007, A&A, 476, 1019

Muñoz Caro, G. M., Chen, Y.-J., Aparicio, S., et al. 2016, A&A, 589, A19

Muñoz Caro, G. M., Jiménez-Escobar, A., Martín-Gago, J. Á., et al. 2010, A&A, 522, A108

Narayanan, D., Krumholz, M., Ostriker, E. C., & Hernquist, L. 2011, MNRAS, 418, 664

Narayanan, D., & Krumholz, M. R. 2014, MNRAS, 442, 1411

Nazé, Y., Rauw, G., Sana, H., & Corcoran, M. F. 2013, A&A, 555, A83

Noble, J. A., Congiu, E., Dulieu, F., & Fraser, H. J. 2012, MNRAS, 421, 768

Nürnberger, D. E. A., & Stanke, T. 2003, A&A, 400, 223

Öberg, K. I., van Dishoeck, E. F., & Linnartz, H. 2009, A&A, 496, 281

Okamoto, R., Yamamoto, H., Tachihara, K., et al. 2017, ApJ, 838, 132

Olnon, F. M., Raimond, E., Neugebauer, G., et al. 1986, A&AS, 65, 607

Peñaloza, C. H., Clark, P. C., Glover, S. C. O., Shetty, R., & Klessen, R. S. 2017, MNRAS, 465, 2277

Peretto, N., Fuller, G. A., Plume, R., et al. 2010, A&A, 518, L98

Pineda, J. E., Caselli, P., & Goodman, A. A. 2008, ApJ, 679, 481

Pineda, J. L., Goldsmith, P. F., Chapman, N., et al. 2010, ApJ, 721, 686

Pineda, J. L., Langer, W. D., Velusamy, T., & Goldsmith, P. F. 2013, A&A, 554, A103

Pitts, R. L., Barnes, P. J., Ryder, S. D., & Li, D. 2018, ApJL, 867, L7

Pitts, R. L., Barnes, P. J., & Varosi, F. 2019, MNRAS, 484, 305

Planck Collaboration, Ade, P. A. R., Aghanim, N., et al. 2011, A&A, 536, A23

Poglitsch, A., Waelkens, C., Geis, N., et al. 2010, A&A, 518, L2

Povich, M. S., Smith, N., Majewski, S. R., et al. 2011, ApJS, 194, 14

Preibisch, T., Mehlhorn, M., Townsley, L., Broos, P., & Ratzka, T. 2014, A&A, 564, A120

Rathborne, J. M., Brooks, K. J., Burton, M. G., Cohen, M., & Bontemps, S. 2004, A&A, 418, 563

Reach, W. T., Heiles, C., & Bernard, J.-P. 2015, ApJ, 811, 118

Reach, W. T., Koo, B.-C., & Heiles, C. 1994, ApJ, 429, 672

Reid, M. J., Menten, K. M., Zheng, X. W., et al. 2009, ApJ, 700, 137

Rieke, G. H., Young, E. T., Engelbracht, C. W., et al. 2004, ApJS, 154, 25

Ripple, F., Heyer, M. H., Gutermuth, R., Snell, R. L., & Brunt, C. M. 2013, MNRAS, 431, 1296

Rodgers, A. W., Campbell, C. T., & Whiteoak, J. B. 1960, MNRAS, 121, 103

Scalise, E., Rodriguez, L. F., J., & Mendoza-Torres, E. 1989, A&A, 221, 105

Schaller, G., Schaerer, D., Meynet, G., & Maeder, A. 1992, A&AS, 96, 269

Schap, W. J., Barnes, P. J., Ordoñez, A., et al. 2017, MNRAS, 465, 2559

Schmidt, M. 1959, ApJ, 129, 243

Schmidt, M. 1963, ApJ, 137, 758

Schutte, A. J., van der Walt, D. J., Gaylard, M. J., & MacLeod, G. C. 1993, MNRAS, 261, 783

Shetty, R., Glover, S. C., Dullemond, C. P., et al. 2011a, MNRAS, 415, 3253

Shetty, R., Glover, S. C., Dullemond, C. P., & Klessen, R. S. 2011b, MNRAS, 412, 1686

Simpson, R. J., Povich, M. S., Kendrew, S., et al. 2012, MNRAS, 424, 2442

Siringo, G., Kreysa, E., Kovács, A., et al. 2009, A&A, 497, 945

Smith, N., Bally, J., & Walborn, N. R. 2010, MNRAS, 405, 1153

Smith, N., Stassun, K. G., & Bally, J. 2005, AJ, 129, 888

Sofue, Y., & Kohno, M. 2020, MNRAS, 497, 1851

Stahler, S. W., & Palla, F. 2005, The Formation of Stars (Weinheim: Wiley-VCH), 865

Sung, H., & Bessell, M. S. 2004, AJ, 127, 1014

Tafalla, M., Usero, A., & Hacar, A. 2021, A&A, 646, A97

The, P. S. 1966, CoBos, 35, 1

van der Walt, D. J., Gaylard, M. J., & MacLeod, G. C. 1995, A&AS, 110, 81

Wada, K., Fukushige, R., Izumi, T., & Tomisaka, K. 2018, ApJ, 852, 88

Walsh, A. J., Hyland, A. R., Robinson, G., & Burton, M. G. 1997, MNRAS, 291, 261

Williams, J. P., de Geus, E. J., & Blitz, L. 1994, ApJ, 428, 693

Wilson, T. L., Mezger, P. G., Gardner, F. F., & Milne, D. K. 1970, A&A, 6, 364

Wolfire, M. G., Hollenbach, D., & McKee, C. F. 2010, ApJ, 716, 1191

Wray, J. D. 1966, PhD thesis, Northwestern Univ.

Wright, E. L., Eisenhardt, P. R. M., Mainzer, A. K., et al. 2010, AJ, 140, 1868

Xu, D., Li, D., Yue, N., & Goldsmith, P. F. 2016, ApJ, 819, 22

Yonekura, Y., Asayama, S., Kimura, K., et al. 2005, ApJ, 634, 476

Yusof, N., Hirschi, R., Meynet, G., et al. 2013, MNRAS, 433, 1114

Zinnecker, H., & Yorke, H. W. 2007, ARAA, 45, 481

Zubko, V., Dwek, E., & Arendt, R. G. 2004, ApJS, 152, 211